Co^{II} Immobilized on Aminated Magnetic-Based Metal–Organic Framework: An Efficient Heterogeneous Nanostructured Catalyst for the C–O Cross-Coupling Reaction in Solvent-Free Conditions

Arezou Mohammadinezhad[1] · **Batool Akhlaghinia**[1]

Abstract

In this paper, we report the synthesis of Fe$_3$O$_4$@AMCA-MIL53(Al)-NH$_2$-Co^{II} NPs based on the metal–organic framework structures as a magnetically separable and environmentally friendly heterogeneous nanocatalyst. The prepared nanostructured catalyst efficiently promotes the C–O cross-coupling reaction in solvent-free conditions without the need for using toxic solvents and/or expensive palladium catalyst.

Graphic Abstract
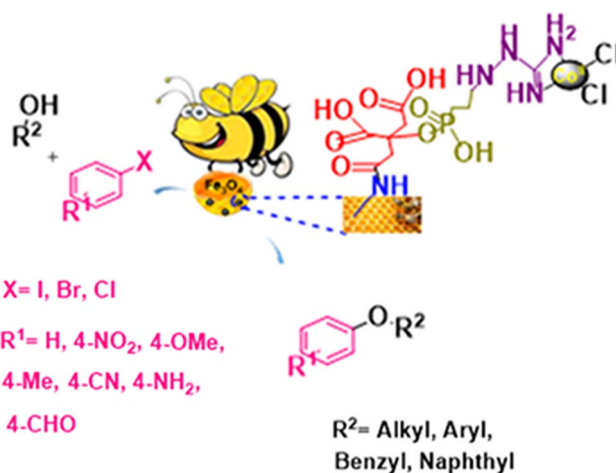
Keywords Co^{II} immobilized on aminated magnetic-based metal–organic framework (Fe$_3$O$_4$@AMCA-MIL53(Al)-NH$_2$-Co^{II} NPs) · C–O cross-coupling reaction · Solvent-free

✉ Batool Akhlaghinia
akhlaghinia@um.ac.ir

1 Department of Chemistry, Faculty of Science, Ferdowsi University of Mashhad, 9177948974 Mashhad, Iran

1 Introduction

Over the past decades, the formation of C–O bond via cross-coupling reactions is one of the most important reactions in organic synthesis [1, 2]. The cross-coupling reactions could be considered as a powerful technique in the synthesis of numerous compounds in biological, biochemical, pharmaceutical, and material interests on both laboratory and industrial scales. In this context, transition-metal-catalyzed cross-coupling reactions have emerged as a versatile strategy

for chemical synthesis as one of the most valued synthetic methodologies for the generation of C–O bond [3–12]. To date, among the various synthetic methods for the formation of C–O bond, the copper-assisted Ullmann type reactions have proven to be the most useful processes due to the low toxicity and low cost of copper [13–15]. During the last century, this coupling reaction found a large number of applications in both the academy and industry and also received considerable attention from the synthetic community [16–18]. However, many drawbacks (including long reaction time, high reaction temperatures at often 150 °C or as high as 200 °C, strong bases, the stoichiometric demand for copper reagents, low tolerance towards functional groups and moderate yields) prevented the further development of these methods for a long time [19, 20]. The vast majority of the other established protocols involved using palladium [21], nickel [22], and iron catalysts [23] to catalyze the C–O cross-coupling reaction. Despite the significant improvements made in the above-mentioned transition-metal catalyzed cross-coupling reactions, the toxic effects along the high costs associated with many transition metals led to an increased interest to develop new and environmentally friendly protocols for the formation of C–O bond using inexpensive and more sustainable metal catalysts immobilized onto support. The supported catalysts facilitate the isolation and recycling of the catalysts and provide environmentally cleaner processes as well [24–29]. Considering that the high surface area of nanostructured material enhances the catalytic activity (via increasing its active sites) and also to circumvent the difficulty imposes in catalyst separation from the reaction media (due to more dispersion of the nano-sized catalyst in solution and hence formation an emulsion), one solution is to employ magnetic nanoparticles as support or catalyst. Interestingly, the magnetic nanostructured materials can be dispersed or aggregated which allows the facile separation and recycling of immobilized catalysts on the nano-sized supports by applying an external magnetic field [30–32]. Among the alternative metal catalysts, immobilization of cobalt salts on the surface of magnetic support has recently attracted keen interest due to its low cost, stability, availability and environmentally benign nature [33, 34]. It provided a new and promising strategy in the area of C–O cross-coupling reaction. Very recently, we have reported an environmentally-friendly magnetic nanostructured catalyst based on Co^{II} for the C–C cross-coupling reactions [34]. In this study, in order to pursue our interests in the preparation and application of heterogeneous catalytic systems based on magnetic nanostructured catalysts in organic transformations [34–38], we have succeeded in innovating Co^{II} immobilized on aminated magnetic-based metal–organic framework Fe_3O_4@AMCA-MIL53(Al)-NH_2 as a new highly efficient magnetically separable catalyst in C–O cross-coupling reaction in solvent-free conditions.

2 Experimental

2.1 General

The purity determinations of the products and the progress of the reactions were accomplished by TLC on silica gel polygram STL G/UV 254 plates and GC-FID (Agilent 6890, Santa Clara, USA) device. The FT-IR spectra were recorded on an Avatar 370 FT-IR Therma Nicolet spectrometer. Elemental analyses were performed using a Thermo Finnigan Flash EA 1112 Series instrument (furnace: 900 °C, oven: 65 °C, flow carrier: 140 mL min^{-1}, flow reference: 100 mL min^{-1}). X-ray powder diffraction (XRD) was performed on a PANalytical Company X'Pert Pro MPD diffractometer with Cu K_{α} radiation ($\lambda = 0.154$ nm) radiation. BET surface area and pore size distribution were measured on a Belsorp mini II system at – 196 °C using N_2 as the adsorbate. Transmission electron microscopy (TEM) was performed with a Leo 912 AB (120 kV) microscope (Zeiss, Germany). FE-SEM images were recorded using a TESCAN, Model: MIRA3 scanning electron microscope operating at an acceleration voltage of 30.0 kV (manufactured by the Czech Republic). Elemental compositions were determined with an SC7620 energy-dispersive X-ray analysis (EDX) and EDX-mapping presenting a 133 eV resolution at 20 kV. Thermogravimetric analyses (TGA) were carried out using a SDT Q600 V20.9 Build 20 in the temperature range of 25–950 °C at a heating rate of 10 °C min^{-1}, under air atmosphere. X-ray photoelectron spectroscopy (XPS) was performed using the Thermo Scientific, ESCALAB 250 Xi Mg X-ray resource. The magnetic property of catalyst was measured using a vibrating sample magnetometer (VSM, Magnetic Danesh Pajoh Inst). UV–Vis. DRS spectra were determined by PerkineElmer, Lambda 25 instrument. Inductively coupled plasma optical emission spectroscopy (ICP-OES) was carried out on a 76,004,555 SPECTRO ARCOS ICP-OES analyzer. All yields refer to the isolated products after purification by thin layer chromatography.

2.2 Preparation of NH_2-MIL53(Al)(I)

2-Aminoterephthalic acid (NH_2-BDC) (5 mmol, 0.905 g) and $AlCl_3 \cdot 6H_2O$ (5 mmol, 1.207 g) were dissolved separately in a solution of deionized water (1.5 mL) and DMF (13.5 mL), respectively. It should be noted that the total volume of solvents must be kept constant at 30 mL. These two distinct solutions were mixed into a 100 mL Teflon-lined steel autoclave and kept in an oven at 150 °C for 24 h under stationary conditions. After cooling to room temperature, the yellow solid product was isolated by

centrifugation. Afterwards, the obtained solid product was in turn boiled in DMF for 5 h (to remove the remained water molecules or unreacted reagents), [39] and then in CH$_3$OH overnight. Finally, the resulting solid NH$_2$-MIL53(Al)(**I**) was collected and dried in an oven at 100 °C overnight [40].

2.3 Preparation of AMCA-MIL53(Al)(II)

NH$_2$-MIL53(Al)(**I**) (2 mmol, 0.418 g) was dispersed in a solution of dicyclohexylcarbodiamide (DCC) (8.71 mmol,1.79 g) and citric acid (8.61 mmol, 1.809 g) in 40 mL acetonitrile. (At first NH$_2$-MIL53(Al)(**I**) was activated by placing in an oven at 150 °C overnight to remove all the adhered DMF in the pores and then cooled to room temperature). The resulting suspension was refluxed for 24 h. The obtained AMCA-MIL53(Al)(**II**) was filtered, washed in turn with DMF (20 mL), CH$_3$CN (20 1 mL) and H$_2$O (20 mL) before drying at 130 °C for three days [41, 42].

2.4 Preparation of Fe$_3$O$_4$@AMCA-MIL53(Al) NPs(III)

AMCA-MIL53(Al)(**II**) (0.4 g) was initially dispersed in deionized water (50 mL) for 30 min. Thereupon, FeCl$_2$·4H$_2$O (4.3 mmol, 0.854 g) and FeCl$_3$·6H$_2$O (8.7 mmol, 2.35 g) were added to the resulting suspension. The mixture was stirred under N$_2$ atmosphere for 3 h. Subsequently, the NH$_3$ solution (25%, 20 mL) was added very slowly and the obtained black mixture was continuously stirred for 1 h under N$_2$ atmosphere. Finally, Fe$_3$O$_4$@AMCA-MIL53(Al) NPs(**III**) were separated by an external magnetic field, washed with deionized water until its pH became neutral and dried at 70 °C for 24 h [42].

2.5 Preparation of Fe$_3$O$_4$@ AMCA-MIL53 (Al)-Ethephon(IV)

Fe$_3$O$_4$@AMCA-MIL53(Al) NPs(**III**) (0.5 g) was dispersed in dry toluene (20 mL) for 30 min. Then, 2-chloroethylphosphonic acid (Ethephon) (2.5 mmol, 0.361 g) was added to the resulting suspension. The mixture was refluxed for 28 h. After that, Fe$_3$O$_4$@AMCA-MIL53(Al)-Ethephon(**IV**) was collected by an external magnet, washed with toluene (5 × 10 mL) and dried in an oven at 50 °C overnight. The loading amount of Cl atom was 0.42 mmol per gram of catalyst based on elemental analysis and TGA.

2.6 Preparation of Fe$_3$O$_4$@AMCA-MIL53(Al)-NH$_2$(V)

Fe$_3$O$_4$@AMCA-MIL53(Al)-Ethephon(**IV**) (0.5 g) was dispersed in dry toluene (20 mL) by placing in an ultrasonic bath for 30 min. Subsequently, amino guanidine nitrate (2.5 mmol, 0.342 g) and sodium bicarbonate (5 mmol,

0.42 g) were added to the suspension and the mixture was refluxed for 48 h. The obtained Fe$_3$O$_4$@AMCA-MIL53(Al)-NH$_2$(**V**) was separated by magnetic decantation, washed with ethanol (5 × 10 mL) and dried at 50 °C overnight. The loading amount of NH$_2$ was 0.41 mmol per gram of catalyst based on elemental analysis and TGA.

2.7 Preparation of Fe$_3$O$_4$@ AMCA-MIL53 (Al)-NH$_2$-Co^{II} NPs(VI)

Fe$_3$O$_4$@AMCA-MIL53(Al)-NH$_2$(**V**) (0.5 g) was dispersed in a solution of CoCl$_2$·6H$_2$O (2.5 mmol, 0.594 g) in absolute EtOH (20 mL) by placing in an ultrasonic bath for 30 min. The resultant suspension was stirred at 60 °C for 18 h. Afterwards, Fe$_3$O$_4$@AMCA-MIL53(Al)-NH$_2$-Co^{II} NPs(**VI**) was collected by a magnetic bar, washed with EtOH (5 × 10 mL) before drying at 50 °C overnight. The loading amount of Co was 0.43 mmol per gram of catalyst based on ICP-OES.

2.8 Typical Procedure for C–O Cross-Coupling Reaction

A round bottom glass tube was charged by phenol (1 mmol, 0.094 g), iodobenzene (1 mmol, 0.203 g), NaOH (3 mmol, 0.12 g), and Fe$_3$O$_4$@AMCA-MIL53(Al)-NH$_2$-Co^{II} NPs(**VI**) (1.08 mol%, 0.04 g). The reaction mixture was stirred at 90 °C under solvent free conditions. Thin layer chromatography (TLC) or gas chromatography (GC) were used to monitor the progress of the reaction. After completion of the reaction (6h), the reaction mixture was quenched by addition of 2 mL ethyl acetate. The nanostructured catalyst was separated using an external magnetic field, washed with ethanol and water before drying in an oven at 50 °C overnight for the next run use. The obtained crude product was purified by thin layer chromatography using *n*-hexane/ethyl acetate (50:1) to afford the pure diphenyl ether (0.161 g, 95% yield).

3 Results and Discussion

In the first part of this paper, the preparation of Fe$_3$O$_4$@AMCA-MIL53(Al)-NH$_2$-Co^{II} NPs was described along with the analytical and spectroscopic evidence which were provided by the following analysis including Fourier transform infrared spectroscopy (FT-IR), X-ray powder diffraction (XRD), Brunauer, Emmett and Teller (BET) surface area analysis, transmission electron microscopy (TEM), field emission scanning electron microscopy (FE-SEM), energy-dispersive X-ray (EDX), energy-dispersive X-ray (EDX) elemental mapping, thermogravimetric analysis (TGA), X-ray photoelectron spectroscopy (XPS), vibrating sample magnetometer (VSM), inductively coupled plasma optical emission spectroscopy (ICP-OES), and elemental

analysis (CHN). In the second part, we illustrated the catalytic activity of Fe₃O₄@AMCA-MIL53(Al)-NH₂-Co^{II} NPs in C–O cross-coupling reaction in solvent-free conditions.

3.1 Catalyst Preparation and Characterization

The preparation of Fe₃O₄@AMCA-MIL53(Al)-NH₂-Co^{II} NPs was performed in a stepwise manner according to the strategy reported by Alqadami et al. [40] (Scheme 1).
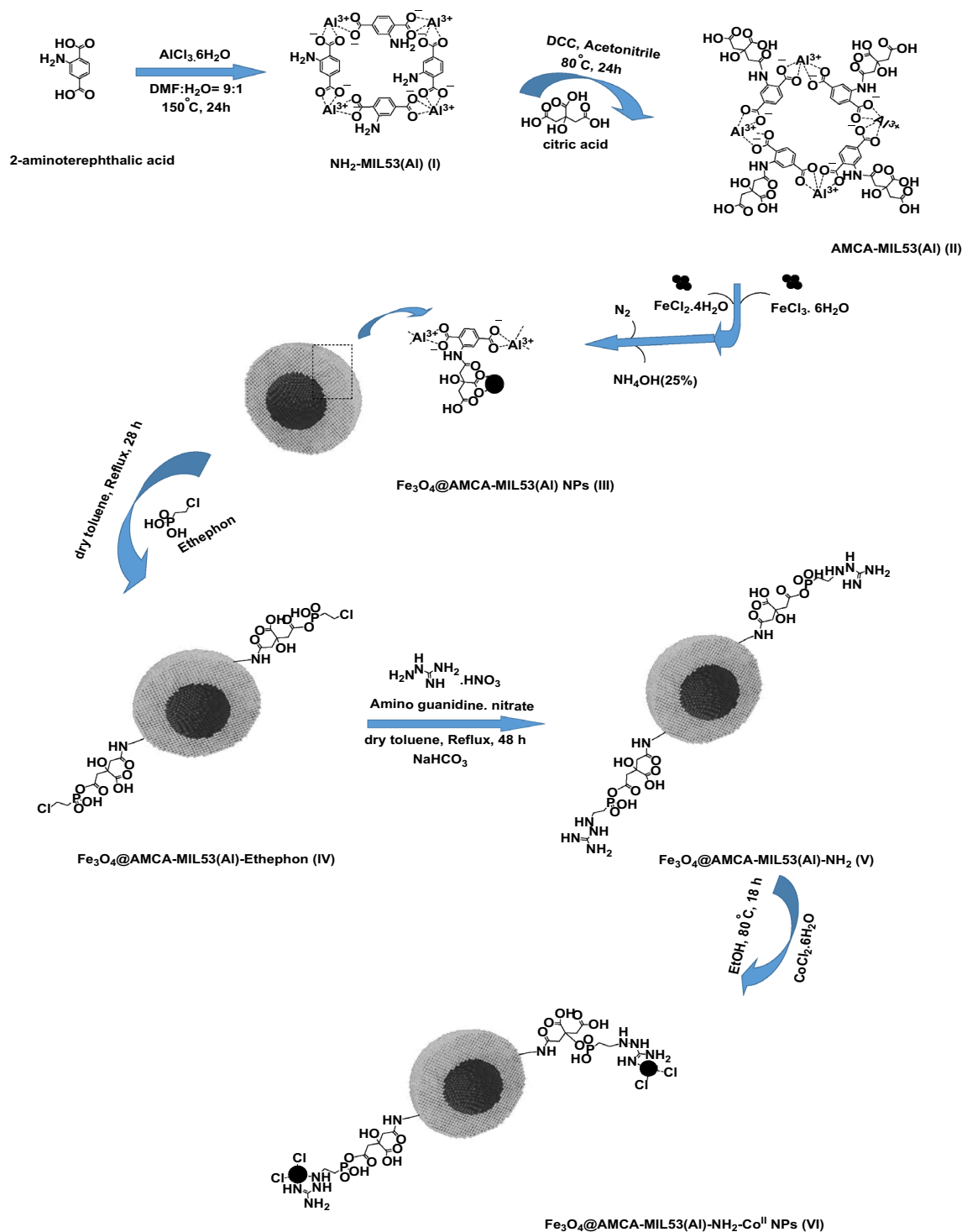
Scheme 1 The synthetic route for the preparation of Fe₃O₄@AMCA-MIL53(Al)-NH₂-Co^{II} NPs(**VI**)

This multistep preparation method consists of the solvothermal route to synthesize NH$_2$-MIL53(Al)(**I**) framework. Metal–organic frameworks (MOFs) were constructed from the coordination of metal ions or clusters with organic linkers via covalent bonds [41–44]. Due to their ability to stabilize nanoparticles without blocking their surfaces, MOFs have attracted an intense attention in the field of catalysis which has made them a viable candidate "shell" to encapsulate the magnetic core [45–49]. To this end, 2-aminoterephthalic acid (NH$_2$-BDC) as the organic linker reacted with AlCl$_3$·6H$_2$O as the metal source at 150 °C. The obtained yellow solid NH$_2$-MIL53(Al)(**I**) (MOF) was refluxed in DMF for 5 h to remove the remaining water molecules or unreacted reactants. Subsequent boiling of NH$_2$-MIL53(Al) (**I**) in CH$_3$OH (as a more volatile solvent) and placing it in an oven at 150 °C overnight, removed the adhered DMF in the pores. Afterward, upon the reaction of the activated NH$_2$-MIL53(Al)(**I**) with citric acid in the presence of dicyclohexylcarbodiamide (DCC), AMCA-MIL53(Al)(**II**) was obtained as a pale yellow solid. In the following step, the magnetization of AMCA-MIL53(Al)(**II**) was performed by treatment with FeCl$_2$·4H$_2$O and FeCl$_3$·6H$_2$O in the presence of ammonia solution. As the hydroxyl groups on the structure of the prepared Fe$_3$O$_4$@AMCA-MIL53(Al) NPs(**III**) are available sites to react with different linkers and ligands, functionalization of Fe$_3$O$_4$@AMCA-MIL53(Al) NPs(**III**) was performed by treatment with 2-chloroethyl phosphonic acid (Ethephon). Further reaction with aminoguanidine nitrate affords Fe$_3$O$_4$@AMCA-MIL53(Al)-Ethephon(**IV**) and Fe$_3$O$_4$@AMCA-MIL53(Al)-NH$_2$(**V**) respectively. By providing extra active sites for immobilization of metal ions and with particular emphasis on the low cost, stability, availability and environmentally benign nature of Co^{II} salts, the Co^{II} immobilized on aminated magnetic-based metal–organic framework [Fe$_3$O$_4$@AMCA-MIL53(Al)-NH$_2$-Co^{II} NPs(**VI**)] was gained after the reaction of the ethanolic solution of CoCl$_2$·6H$_2$O with Fe$_3$O$_4$@AMCA-MIL53(Al)-NH$_2$(**V**).

In order to confirm the chemical structure of NH$_2$-MIL53(Al)(**I**), AMCA-MIL53(Al)(**II**), Fe$_3$O$_4$@AMCA-MIL53(Al) NPs(**III**), Fe$_3$O$_4$@AMCA-MIL53(Al)-Ethephon(**IV**), Fe$_3$O$_4$@AMCA-MIL53(Al)-NH$_2$(**V**), and Fe$_3$O$_4$@AMCA-MIL53(Al)-NH$_2$-Co^{II} NPs(**VI**), the Fourier transform infrared (FT-IR) spectroscopy was utilized and the results are shown in Fig. 1. The free NH$_2$ groups are responsible for the appearance of two sharp bands at 3498 and 3388 cm^{-1} (Fig. 1a). In addition, the absorption bands related to the stretching vibration frequencies of the OH (octahedral AlO$_4$(OH)$_2$) and=C–CH groups are located at 3628 and 3048 cm^{-1}, respectively [50]. Likewise, the existence of carboxylate groups coordinated with Al^{3+} ions was confirmed via the presence of characteristic absorption bands at 1620, 1499, 1442 and 1395 cm^{-1} which correspond to the
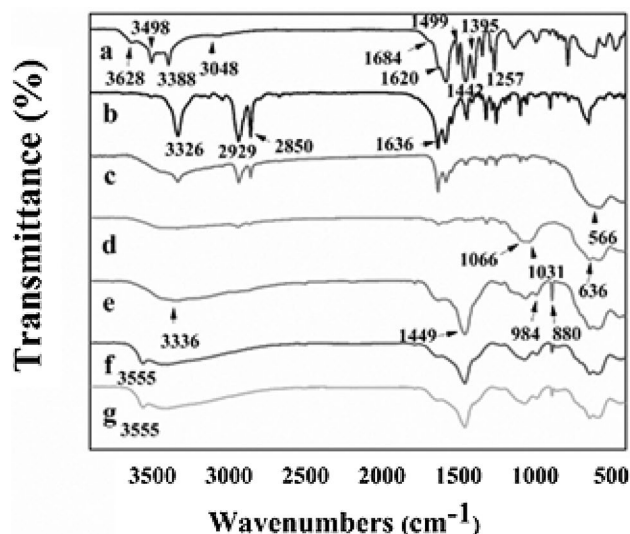

Fig. 1 FT-IR spectra of NH$_2$-MIL53(Al)(**I**) (a), AMCA-MIL53(Al) (**II**) (b), Fe$_3$O$_4$@AMCA-MIL53(Al) NPs(**III**) (c), Fe$_3$O$_4$@AMCA-MIL53(Al)-Ethephon(**IV**) (d), Fe$_3$O$_4$@AMCA-MIL53(Al)-NH$_2$(**V**) (e), Fe$_3$O$_4$@ AMCA-MIL53(Al)-NH$_2$-Co^{II} NPs(**VI**)(f) and the 7th reused Fe$_3$O$_4$@ AMCA-MIL53(Al)-NH$_2$-Co^{II} NPs(**VI**) (g)

asymmetric and symmetric stretching vibrations of carboxylate groups [39]. Furthermore, a week absorption band at 1684 cm^{-1} can be assigned to the DMF trapped within the MOF porous [40, 43, 50]. The absorption band at 1257 cm^{-1} which is ascribed to the C-N vibration, confirming the existence of amino groups in the MOF structure (Fig. 1a). In the case of AMCA-MIL53(Al)(**II**), the formation of amide linkage (Co–NH) in the framework structure can be established according to the attendance of a new absorption band at 1636 cm^{-1} (Fig. 1b) [51]. Figure 1c displays a distinctive band at 566 cm^{-1} which is indexed to the Fe–O vibration of Fe$_3$O$_4$ NPs (Fig. 1c) [52]. Successful grafting of Ethephon on the surface of Fe$_3$O$_4$@AMCA-MIL53(Al) NPs(**III**) was corroborated by the apparition of three new bands at 1066, 1031, and 636 cm^{-1} related to the stretching vibrations of P=O and also symmetric and bending vibrations of O–P–O bonds, respectively (Fig. 1d). In the FT-IR spectrum of Fe$_3$O$_4$@AMCA-MIL53(Al)-NH$_2$(**V**) (Fig. 1e), the absorption bands emerged at 3336 and 1449 cm^{-1} are assigned to the N–H and C-N stretching vibrations of aminoguanidine grafted on the surface of Fe$_3$O$_4$@AMCA-MIL53(Al)-Ethephon(**IV**) [40]. Finally, the intensity of the absorption band of Fe$_3$O$_4$@AMCA-MIL53(Al)-NH$_2$(**V**) was decreased after modification process with Co^{II} species which results from the coordination of Co^{II} ions to the amino groups of Fe$_3$O$_4$@AMCA-MIL53(Al)-NH$_2$(**V**) (Fig. 1f). Notably, a new absorption band at 3555 cm^{-1} was observed, which is in good agreement with the reported literature and can be indicated the presence of the lattice water molecule in the cobalt complex [53, 54].

The phase purity and crystalline structure of NH_2-MIL53(Al)(**I**), Fe_3O_4 MNPs, Fe_3O_4@AMCA-MIL53(Al) NPs(**III**), and Fe_3O_4@AMCA-MIL53(Al)-NH_2-Co^{II} NPs(**VI**) were authenticated through surveying the X-ray diffraction (XRD) patterns. In the pattern assigned to NH_2-MIL53(Al)(**I**) (Fig. 2a), diffraction peaks around $2\theta = 11.02°$ (2 0 0), 15.05° (0 1 1), 17.19 ° (2 0 2), 18.65° (2 1 1, 2 2 0), 28.74° (0 2 0), 41.64° (1 1 1) and 67.2° (2 2 0) are related to the NH_2-MIL53(Al)(**I**) structure [40, 50, 55–59]. The cubic structure of Fe_3O_4 MNPs (Ref. Code: 98–001-7122) can be certified by typical diffraction peaks at $2\theta = 30.53°$, 35.81°, 43.54°, 54.08°, 57.34°, 63.28°, and 74.62° correspond to (2 2 0), (3 1 1), (4 0 0), (4 2 2), (5 1 1), (4 4 0) and (6 2 2) planes, respectively. Two distinct phases can be recognized in the XRD pattern of Fe_3O_4@AMCA-MIL53(Al) NPs(**III**) which are allied to Fe_3O_4 MNPs and NH_2-MIL53(Al)(**I**) (Fig. 2c). It is worth mentioning that the presence of AMCA-MIL53(Al)(**I**) in the structure of Fe_3O_4@AMCA-MIL53(Al) NPs(**III**) can further confirmed by the appearance of four new diffraction peaks at $2\theta = 20.5°$, 21.9°, 22.23° and 31.88°, indicating the presence of citric acid molecules packed in the framework structure [60]. As a result of modification process, the intensities and positions of diffraction peaks were changed. Furthermore, the X-ray diagram of Fe_3O_4@AMCA-MIL53(Al)-NH_2-Co^{II} NPs(**VI**) showed five new diffraction peaks at $2\theta = 32.21°$ (2 2 0), 38.28° (0 2 2), 39.96° (0 3 1), 41.75° (4 0 0, 3 2 1) and 46.02 ° (2 3 1, 4 0 2), indicating the presence of Co^{II} species in the structure of nanostructured catalyst [60]. As a final point, the crystalline size of Fe_3O_4@AMCA-MIL53(Al)-NH_2-Co^{II} NPs(**VI**) was estimated using Debye–Scherrer's equation to be 21 nm.
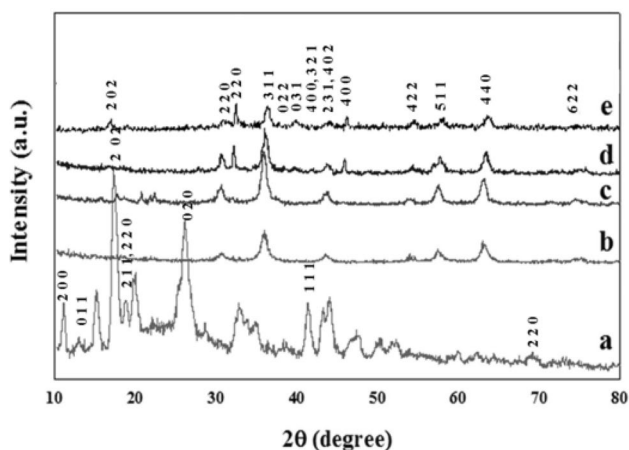
Fig. 2 XRD patterns of NH_2-MIL 53(Al)(**I**) (a), Fe_3O_4 MNPs (b), Fe_3O_4@AMCA-MIL53 (Al) NPs (**III**)(c), Fe_3O_4@AMCA-MIL53 (Al)-NH_2-Co^{II} NPs(**VI**) (d) and the 7th reused Fe_3O_4@ AMCA-MIL53(Al)-NH_2-Co^{II} NPs (**VI**) (e)

The textural properties of NH_2-MIL53(Al)(**I**), Fe_3O_4@AMCA-MIL53(Al) NPs(**III**) and Fe_3O_4@AMCA-MIL53(Al)-NH_2-Co^{II} NPs(**VI**) were measured using nitrogen adsorption–desorption analysis. As can be seen in Fig. 3, all samples show typical type IV isotherms with a H3-type hysteresis loops, reflecting the meso- or microporous structure (Based on IUPAC classification). The derived data including specific surface area, pore volume and mean pore diameter are summarized in Table 1. The BET surface area of NH_2-MIL53(Al)(**I**), Fe_3O_4@AMCA-MIL53(Al) NPs(**III**) and Fe_3O_4@AMCA-MIL53(Al)-NH_2-Co^{II} NPs(**VI**) are calculated to be around 82.95, 99.51 and 69.27, respectively. It should be noted that the BET surface area of NH_2-MIL 53(Al)(**I**) is lower than the number reported in the literature [61–65]. It is interesting to note that due to the entrance of Fe_3O_4 NPs into the framework pores, the BET surface area was increased. Moreover, the specific surface area of Fe_3O_4@AMCA-MIL53(Al)-NH_2-Co^{II} NPs(**VI**) was decreased during modification process as a result of blocking of some pores by organic segments.

The transmission electron microscopy (TEM) was utilized to investigate the size and morphology of Fe_3O_4@AMCA-MIL53(Al)-NH_2-Co^{II} NPs(**VI**). The TEM images and particle size distributions are shown in Figs. 4 and 5. Figure 4 clearly demonstrated the core–shell structure of the as-synthesized nanostructured catalyst with an average size of 10–30 nm (according to the particle size distributions) which is very close to the particle size determined using XRD data.

A more detailed investigation on the shape and morphology of Fe_3O_4@AMCA-MIL53(Al)-NH_2-Co^{II} NPs(**VI**) were obtained by surveying the FE-SEM images. As can be seen in Fig. 6, the as-synthesized nanostructured catalyst exhibit an irregular morphology with good dispersion.

The existence of elements in the Fe_3O_4@AMCA-MIL53(Al)-NH_2-Co^{II} NPs(**VI**) structure was confirmed using the energy-dispersive X-ray (EDX) technique. According to the data which are shown in Fig. 7, C, O, N, P, Fe, Co, Al, and Cl were present in the Fe_3O_4@AMCA-MIL53(Al)-NH_2-Co^{II} NPs(**VI**) composition.

To further evaluate the composition of Fe_3O_4@AMCA-MIL53(Al)-NH_2-Co^{II} NPs(**VI**), the EDX-mapping analysis was performed. As it is evident, the attendance of C, O, N, P, Fe, Co, Al, and Cl was observed with a uniform distribution (Fig. 8).

The thermogravimetric analysis (TGA) was used to investigate the thermal and structural stabilities of NH_2-MIL53(Al)(**I**), AMCA-MIL53(Al)(**II**), Fe_3O_4 NPs, Fe_3O_4@AMCA-MIL53(Al) NPs(**III**), Fe_3O_4@AMCA-MIL53(Al)-Ethephon(**IV**), and Fe_3O_4@AMCA-MIL53(Al)-NH_2-Co^{II} NPs(**VI**). The results are shown in Fig. 9. The TGA thermogram of NH_2-MIL53(Al)(**I**) shows two specific step weight losses from 25 to 600 °C.

Fig. 3 The nitrogen adsorption–desorption isotherms of NH$_2$-MIL53(Al)(**I**) (**a**), Fe$_3$O$_4$@AMCA-MIL53(Al) NPs(**III**) (**b**), Fe$_3$O$_4$@AMCA-MIL53(Al)-NH$_2$-Co^{II} NPs (**VI**) (**c**) and the 7th reused Fe$_3$O$_4$@AMCA-MIL53(Al)-NH$_2$-Co^{II} NPs (**VI**) (**d**)
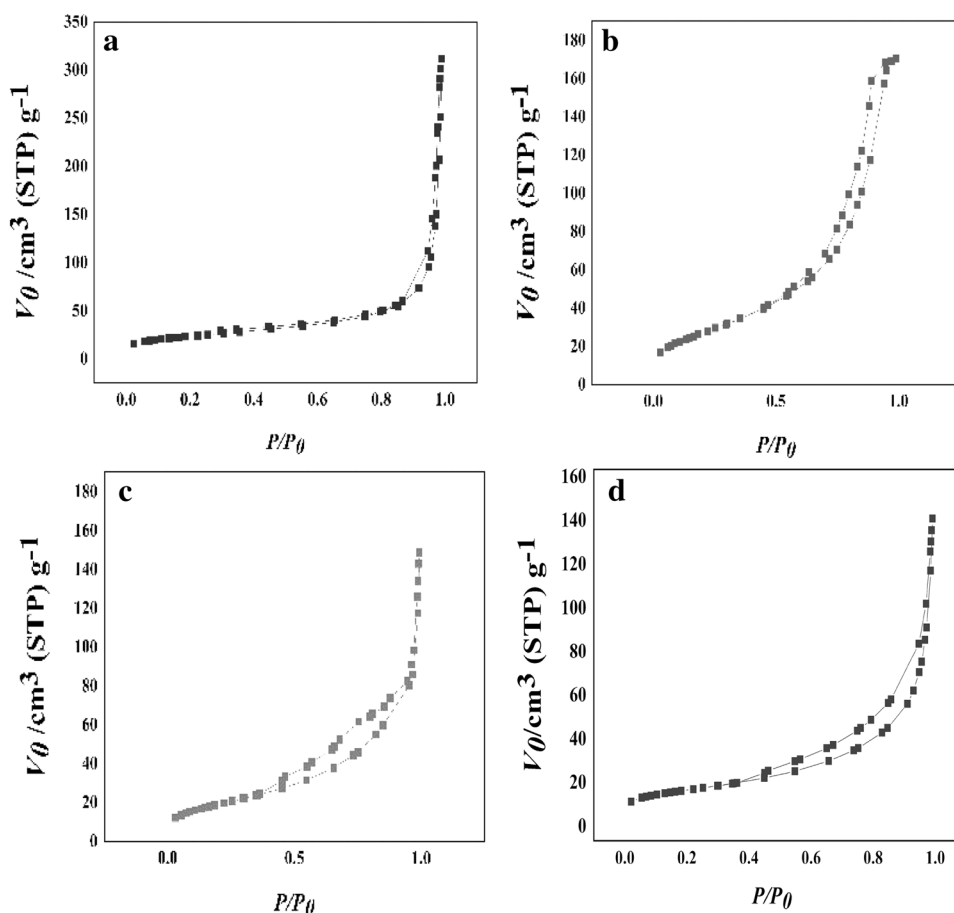

Table 1 Specific surface area (S_{BET}), pore volume and mean pore diameter of NH$_2$-MIL 53(Al) (**I**)(a), Fe$_3$O$_4$@AMCA-MIL53 (Al) NPs(**III**) (b), Fe$_3$O$_4$@AMCA-MIL53 (Al)-NH$_2$-Co^{II} NPs (**VI**) (c) and the 7th reused Fe$_3$O$_4$@ AMCA-MIL53(Al)-NH$_2$-Co^{II} NPs (**VI**) (d)

Samples	S_{BET} (m^{2}g^{-1})	Total pore volume (cm^3 g^{-1})	Mean pore diameter (nm)
NH$_2$-MIL 53 (Al)(**I**)	82.95	0.48	23
Fe$_3$O$_4$@AMCA-MIL53(Al)NPs(**III**)	99.51	0.26	10
Fe$_3$O$_4$@AMCA-MIL53 (Al)-NH$_2$-Co^{II} NPs(**VI**)	69.27	0.20	11
7th reused Fe$_3$O$_4$ @ AMCA-MIL 53(Al)-NH$_2$-CoII NPs(**VI**)	49.5	0.20	17

As can be seen in Fig. 9a, the first observed weight loss (7%) which occurred from 25 to 150 °C, can be related to the release of water molecules from the sample surface and trapped DMF in the pores of NH$_2$-MIL53(Al)(**I**) (Fig. 9a) [57, 66]. The second ones, which is the major weight loss, indicating the decomposition of amino-tere-phthalic acid (NH$_2$-BDC) linker in the region from 350 to 600 °C [41, 57]. The successful formation of amide linkage on the surface of NH$_2$-MIL53(Al)(**I**) was corroborated by the advent of three steps of thermal degra-dation (Fig. 6b). As mentioned previously, the removal of adsorbed water molecules is responsible for the first weight loss (1%) from 25 to 100 °C. Likewise, the collapse

of MOF structure (NH$_2$-BDC groups and grafted citric acid molecules) occurred during the second and third step weight losses from 150 to 600 °C [57]. Figure 9c, which is attributed to the Fe$_3$O$_4$ NPs, displays two-step thermal degradation. As it is evident from Fig. 9c, the physically adsorbed water molecules befell from 25 to 150 °C (1.5% weight loss). Also, the transformation of some hydroxide groups to oxide form and also the elimination of crystal-line water molecules happened during the second weight loss (3%) from 180 to 400 °C [40]. In the case of Fe$_3$O$_4$@ AMCA-MIL53(Al) NPs(**III**), the decomposition pattern is similar to the decomposition patterns of NH$_2$-MIL53(Al) (**I**) and Fe$_3$O$_4$ NPs, indicating the coexistence of magnetic

Fig. 4 TEM images of the fresh Fe$_3$O$_4$@AMCA-MIL53 (Al)-NH$_2$-Co^{II} NPs (**VI**) (**a**, **b**) and the 7th reused Fe$_3$O$_4$@ AMCA-MIL53(Al)-NH$_2$-Co^{II} NPs (**VI**) (**c**)
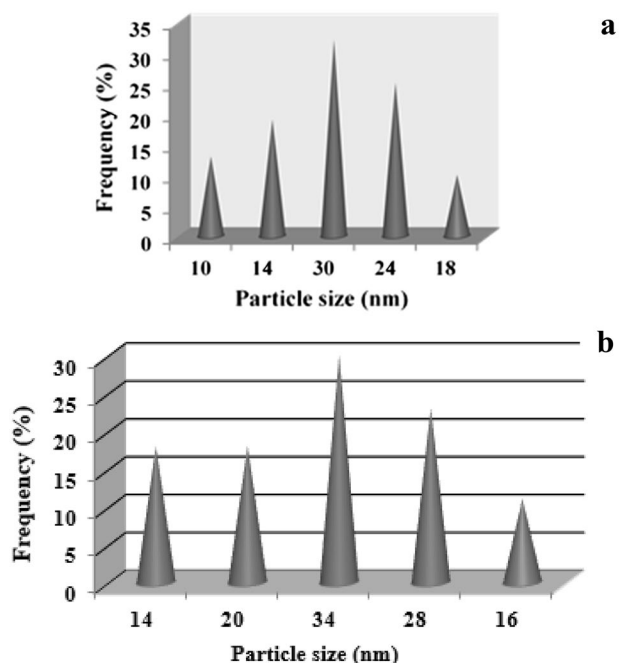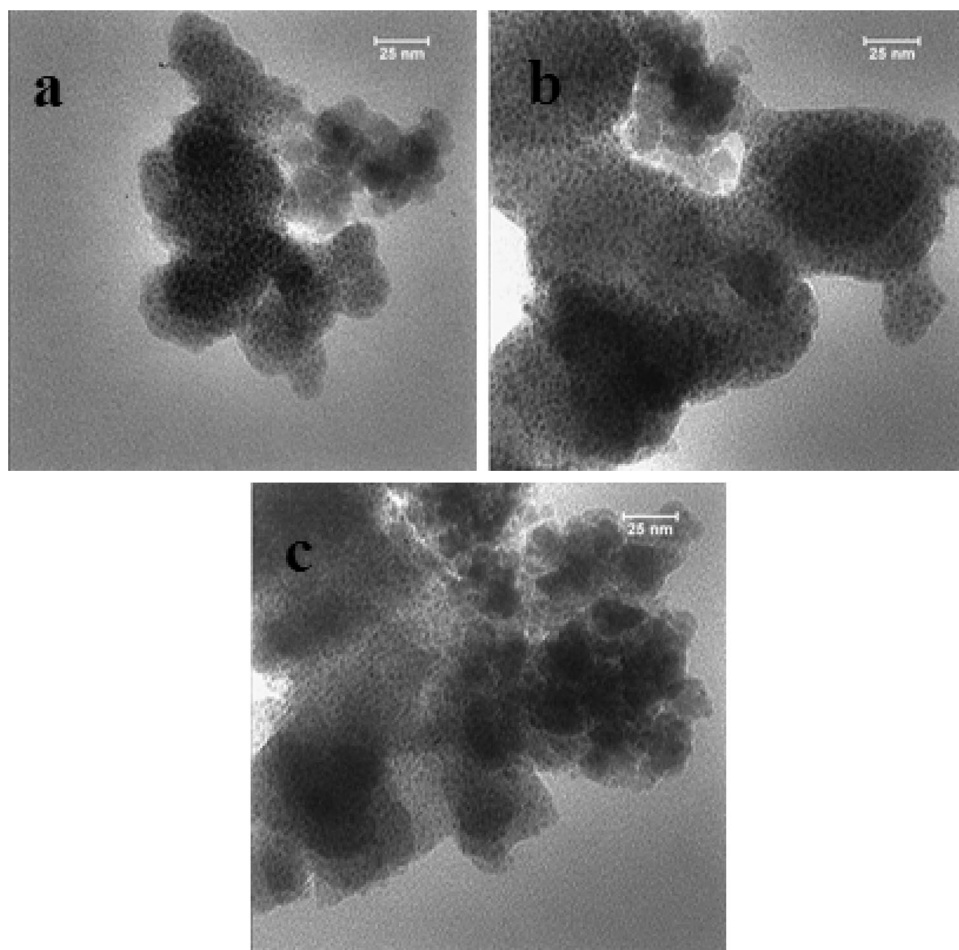
Fig. 5 Particle size distribution histogram of the fresh Fe$_3$O$_4$@ AMCA-MIL53 (Al)-NH$_2$-Co^{II} NPs (**VI**) (**a**) and the 7th reused Fe$_3$O$_4$@ AMCA-MIL53(Al)-NH$_2$-Co^{II} NPs (**VI**) (**b**)

core and MOF shell. The only observed difference can be related to the presence of dense and inorganic Fe$_3$O$_4$ NPs in the structure of MOF which leads to a decrease in weight loss (14%) [67]. The TGA thermogram of Fe$_3$O$_4$@ AMCA-MIL53(Al) NPs(**III**) exhibited three-step weight losses from 25 to 600 °C. As mentioned above, removal of adsorbed water molecules, the transformation of hydroxide groups to oxide form in the Fe$_3$O$_4$ NPs phase and also release of the trapped DMF molecules, and also decomposition of NH$_2$-MIL53(Al)(**I**) framework are responsible for the attendance of first, second and third weight losses, respectively (Fig. 9d). Successful grafted of Ethephon on the surface of Fe$_3$O$_4$@AMCA-MIL53(Al) NPs(**III**) can be confirmed via an increase in the weight loss from 4 to 10% (410 to 600 °C) (Fig. 9e). It is interesting to note that there is no difference in the decomposition pattern of Fe$_3$O$_4$@AMCA-MIL53(Al)-Ethephon(**IV**) and Fe$_3$O$_4$@ AMCA-MIL53(Al)-NH$_2$-Co^{II} NPs(**VI**). The only difference could be related to an increase in the weight loss (3%) from 410 to 600 °C owing to the grafting of aminoguanidine molecules to the Ethephon linkers. Furthermore, the amount of organic moieties on the surface of Fe$_3$O$_4$@ AMCA-MIL53(Al) NPs(**III**) was estimated using TGA

Fig. 6 FE-SEM images of Fe$_3$O$_4$@AMCA-MIL53 (Al)-NH$_2$-Co^{II} NPs(**VI**) (**a–c**) and the 7th reused Fe$_3$O$_4$@ AMCA-MIL53(Al)-NH$_2$-Co^{II} NPs (**VI**) (**d**)
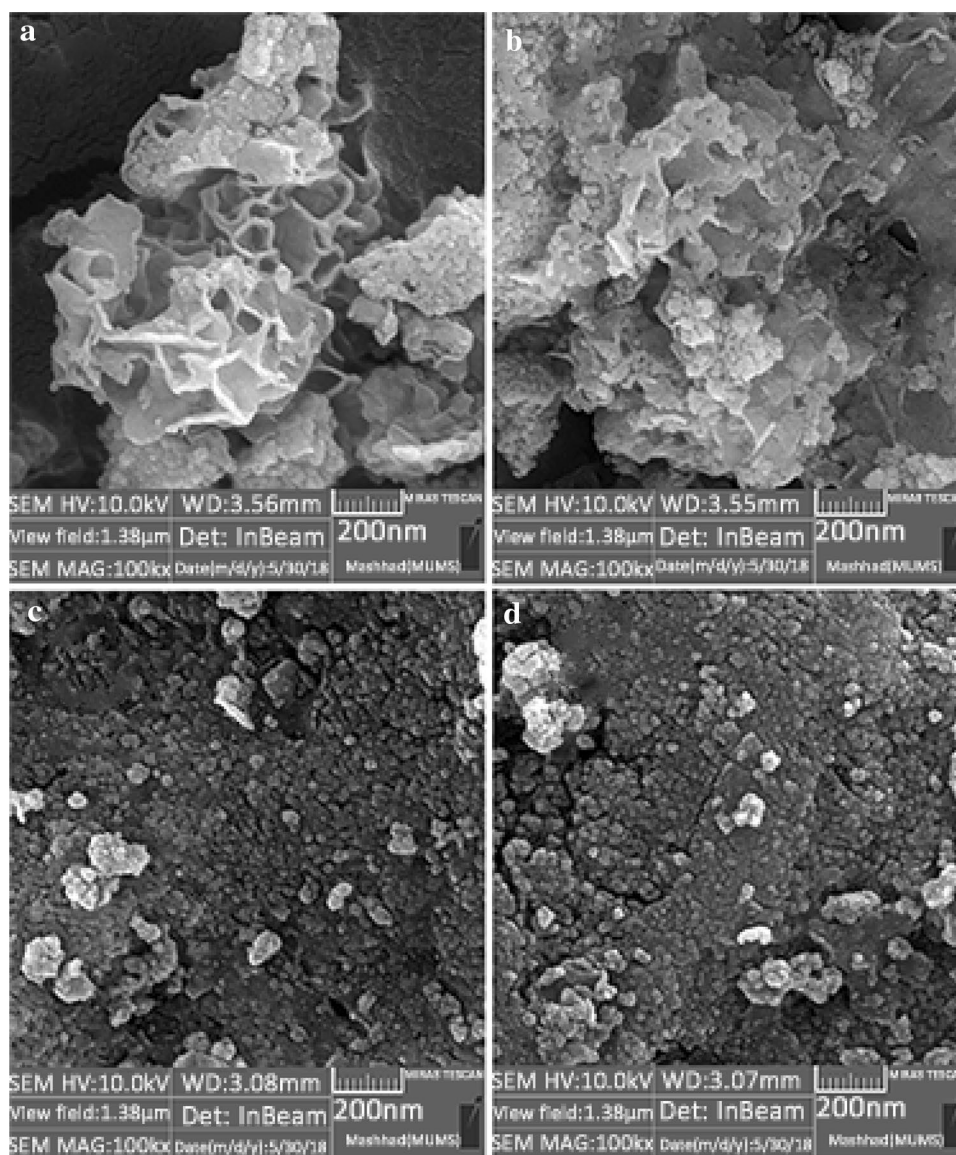
analysis and the results are depicted in Table 2. A good agreement was observed between the elemental analysis and TGA data, according to the obtained results.

To further analyzed the chemical composition and also to estimate the oxidation state of the metal ions (Co species) anchored on the surface of Fe$_3$O$_4$@AMCA-MIL53(Al)-NH$_2$-Co^{II} NPs(**VI**), the X-ray photoelectron spectroscopy (XPS) was employed. The XPS spectra of Fe$_3$O$_4$@AMCA-MIL53(Al)-NH$_2$-Co^{II} NPs(**VI**) and the 7th reused nanostructured catalyst were depicted in Fig. 10. The oxidation state of cobalt ions in the Fe$_3$O$_4$@AMCA-MIL53(Al)-NH$_2$-Co^{II} NPs(**VI**) structure was investigated by screening the XPS spectra (Fig. 10a, b). As can be seen, the presence of two strong satellite bands at the binding energies 786.3 (due to Co 2p$_{3/2}$) and 802.9 eV (due to Co 2p$_{1/2}$) alongside the binding energies 781.4 (due to Co 2p$_{3/2}$) and 797.5 eV (due to

Co 2p$_{1/2}$) confirmed the attendance of Co^{+2} species on the surface of Fe$_3$O$_4$@AMCA-MIL53(Al)-NH$_2$(**V**) (Fig. 10a, b) [68]. Moreover, XPS survey scan indicated the presence of C, O, N, P, Cl, Fe, and Al elements in the nanostructured catalyst composition which is in a good agreement with the EDX and EDX-mapping data (Fig. 10c, d) [69].

The magnetic property of Fe$_3$O$_4$@AMCA-MIL53(Al) NPs(**III**) and Fe$_3$O$_4$@AMCA-MIL53(Al)-NH$_2$-Co^{II} NPs(**VI**) was studied by the vibrating sample magnetometer (VSM) technique. The field dependent magnetization curves are plotted in Fig. 11. As can be concluded from Fig. 11, both samples exhibited superparamagnetic behavior. The saturation magnetization values obtained from the VSM curves are estimated to be 47.1 and 28.05 emu g^{-1} for Fe$_3$O$_4$@AMCA-MIL53(Al) NPs(**III**) and Fe$_3$O$_4$@AMCA-MIL53(Al)-NH$_2$-Co^{II} NPs(**VI**), respectively. The observed decrease in the
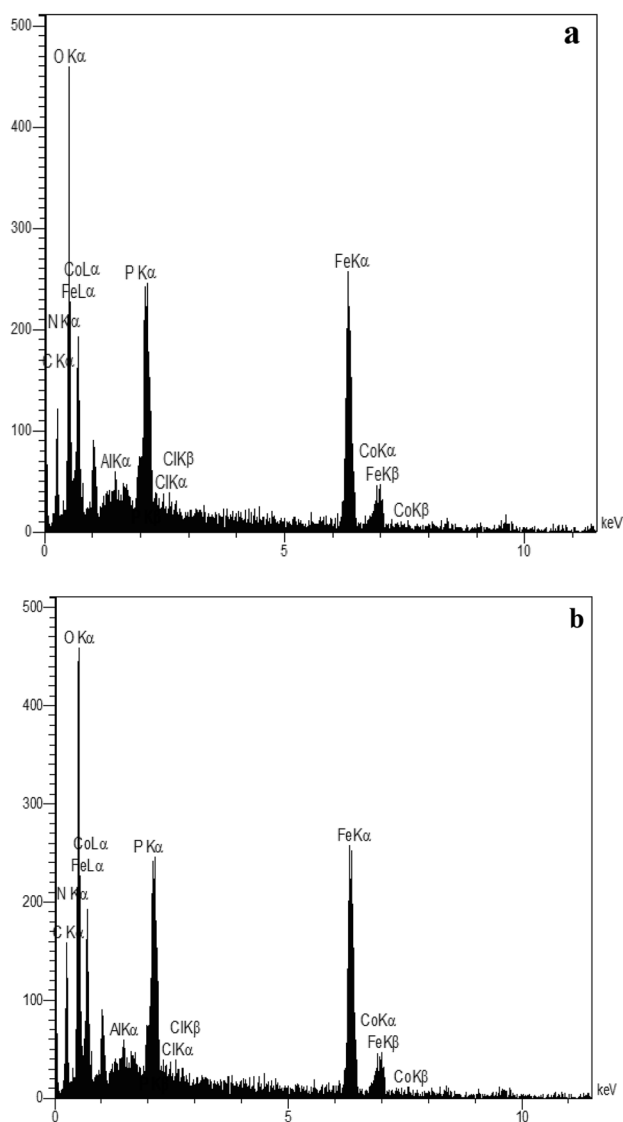
Fig. 7 EDX spectrum of Fe_3O_4@AMCA-MIL53 (Al)-NH_2-Co^{II} NPs (**VI**) (**a**) and the 7th reused Fe_3O_4@ AMCA-MIL53(Al)-NH_2-Co^{II} NPs (**VI**) (**b**)

saturation magnetization (MS) intensity could be attributed to the modification process which leads to the presence of organic segments around Fe_3O_4@AMCA-MIL53(Al) NPs(**III**).

3.2 Catalytic performance of Fe_3O_4@ AMCA-MIL53(Al)-NH_2-Co^{II} NPs(VI) in C–O cross-coupling reaction

After the characterization of this novel core–shell-like nanostructured catalyst, the possibility of Fe_3O_4@AMCA-MIL53(Al)-NH_2-Co^{II} NPs(**VI**) as the active catalyst and initiating the catalytic cycle was tested in C–O cross-coupling reaction as the first report (Scheme 2).

To obtain an optimum reaction profile for the C–O cross-coupling reaction, the cross-coupling reaction of iodobenzene with phenol, was studied as model reaction by taking into consideration various important parameters including solvent, temperature, base, the catalyst loading and the amount of base in the presence of Fe_3O_4@AMCA-MIL53(Al)-NH_2-Co^{II} NPs(**VI**) (Table 3). During our preliminary studies, DMF was used as solvent and K_2CO_3 as the base in the presence of 0.27 mol% of Fe_3O_4@AMCA-MIL53(Al)-NH_2-Co^{II} NPs(**VI**) at 100 °C to evaluate the role of base and catalyst in C–O cross-coupling reaction. Conducting the model reaction in the absence of catalyst and base did not lead to the cross-coupled product even after a long period of time (Table 3, entry 1). The model reaction proceeded far more slowly using only K_2CO_3 as the base (Table 3, entry 2), even after lengthening the reaction time to 24 h, no product was detected in the presence of Fe_3O_4@AMCA-MIL53(Al)-NH_2-Co^{II} NPs(**VI**) without using K_2CO_3 (Table 3, entry 3). Reasonable yield of the desired product (35% after 10 h) in C–O cross-coupling reaction was achieved in the presence of 0.27 mol% of Fe_3O_4@AMCA-MIL53(Al)-NH_2-Co^{II} NPs(**VI**) and using 1/2 molar ratio of iodobenzene/K_2CO_3 which signified the essential catalytic role of nanostructured catalyst and base in the present cross-coupling reaction (Table 3, entry 4). Common solvents, including DMSO, THF, *n*-hexane, toluene, CH_3CN, EtOH, and H_2O as well as solvent-free conditions were tested on model cross-coupling reaction. The solvent-free condition was found to be the suitable medium for the present cross-coupling reaction furnishing the cross-coupled product in higher yield comparatively (Table 3, entries 5–12). Subsequent experiments to identify the effect of temperature (as an important factor for the progress of the reaction) in C–O cross-coupling reaction revealed that the best yield of the desired product was obtained at 90 °C (Table 3, entries 13–16). In order to choose the best base, the model reaction was carried out in the presence of Li_2CO_3, $NaHCO_3$, K_3PO_4, KOH, TETA, NEt_3, ethylenediamine, and NaOH (Table 3, entries 17–24). Among them NaOH was found to be highly efficient for the C–O cross-coupling reaction. Next, the influence of the amount of bases, as well as catalyst loading, were scrutinized using the model reaction to achieve optimal reaction conditions (Table 3, entries 25–30). Further experiments with variable amounts of bases and catalyst loading demonstrated that the cross-coupling reaction proceeded very effectively using 1/3 molar ratio of iodobenzene/base and 1.08 mol% of catalyst in C–O cross-coupling reaction. In a follow-up investigation, the catalytic activity of Fe_3O_4@AMCA-MIL53(Al)-NH_2-Co^{II} NPs(**VI**) was measured in detail by performing the model reaction in the presence of Fe_3O_4NPs, NH_2-MIL53(Al)(**I**), AMCA-MIL53(Al)(**II**), Fe_3O_4@AMCA-MIL53(Al) NPs(**III**), Fe_3O_4@AMCA-MIL53(Al)-Ethephon(**IV**), and Fe_3O_4@

Fig. 8 EDX-mapping of Fe$_3$O$_4$@AMCA-MIL53 (Al)-NH$_2$-Co^{II} NPs(**VI**)
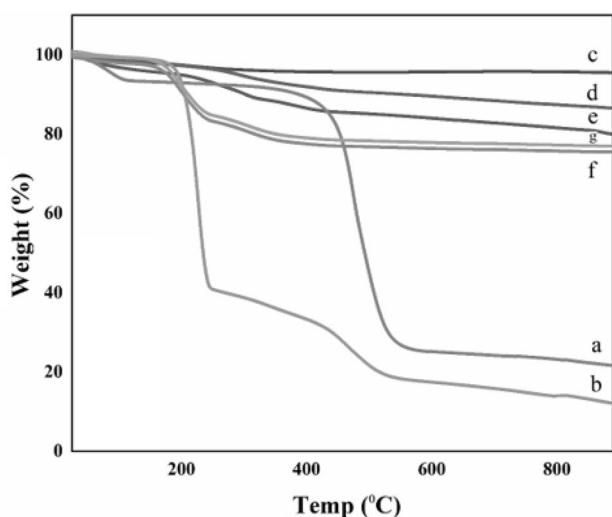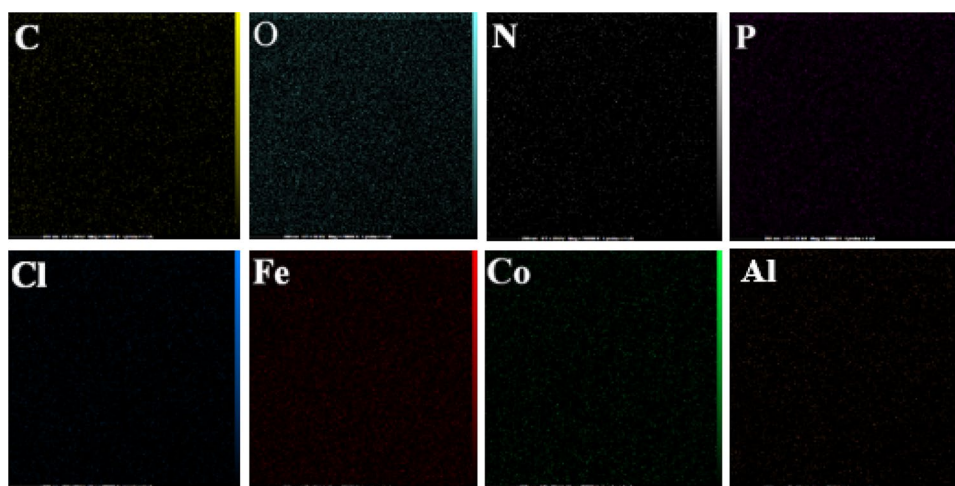
Fig. 9 TGA thermograms of NH$_2$-MIL53(Al)(**I**) (a), AMCA-MIL53(Al)(**II**) (b), Fe$_3$O$_4$ NPs (c), Fe$_3$O$_4$@AMCA-MIL53(Al)(**III**) NPs (d), Fe$_3$O$_4$@AMCA-MIL53(Al)-Ethephon(**IV**) (e), Fe$_3$O$_4$@ AMCA-MIL53(Al)-NH$_2$-Co^{II} NPs(**VI**) (f) and the 7th reused Fe$_3$O$_4$@ AMCA-MIL53(Al)-NH$_2$-Co^{II} NPs (**VI**) (g)

AMCA-MIL53(Al)-NH$_2$(**V**) under the optimized reaction conditions (Table 3, entries 31–36). As expected, the results clearly indicated that a trace amount of the cross-coupled product was obtained in this cross-coupling reaction. Control reaction was also carried out in the presence of both CoCl$_2$·6H$_2$O and CoCl$_2$·6H$_2$O/aminoguanidine, whereby CoCl$_2$·6H$_2$O afforded yield of 0% of desired product in the C–O cross-coupling reaction and 30% of product was obtained when CoCl$_2$·6H$_2$O/aminoguanidine was applied to the same protocol (the combination of an amino ligand with the cobalt species promotes the cross-coupling reaction [70]) (Table 3, entries 37–38).

Moreover, the TOF data was calculated and summarized in Table 3. The reaction parameters including solvent, base, temperature, molar ration of iodobenzene/ base and catalyst loading were investigated on the model reaction in terms of TOF amount. Surveying the effect of solvents leads to find that solvent-free conditions is the suitable medium for the cross-coupling reaction due to its higher TOF amount (Table 3, entries 5–12). In our second screening experiments, the effect of temperature

Table 2 Thermogravimetric analysis (TGA) and elemental analysis (EA) results

Samples	Weight loss (%)	Organic grafted segments (mmol g^{-1})	Elemental analysis (%)	
			C	N
NH$_2$-MIL53(Al)(**I**)	78	–	36	4.5
AMCA-MIL53(Al)(**II**)	88	0.571	60	5
Fe$_3$O$_4$ NPs	4.5	–	–	–
Fe$_3$O$_4$@AMCA-MIL53(Al) NPs(**III**)	14	0.27	3.9	1
Fe$_3$O$_4$@AMCA-MIL53(Al)-Ethephon(**IV**)	20	0.42a	5.5	1
Fe$_3$O$_4$@AMCA-MIL53(Al)-NH$_2$-Co^{II} NPs(**VI**)	23	0.41b	6	2.3

[a]Ethephon

[b]Amino guanidine
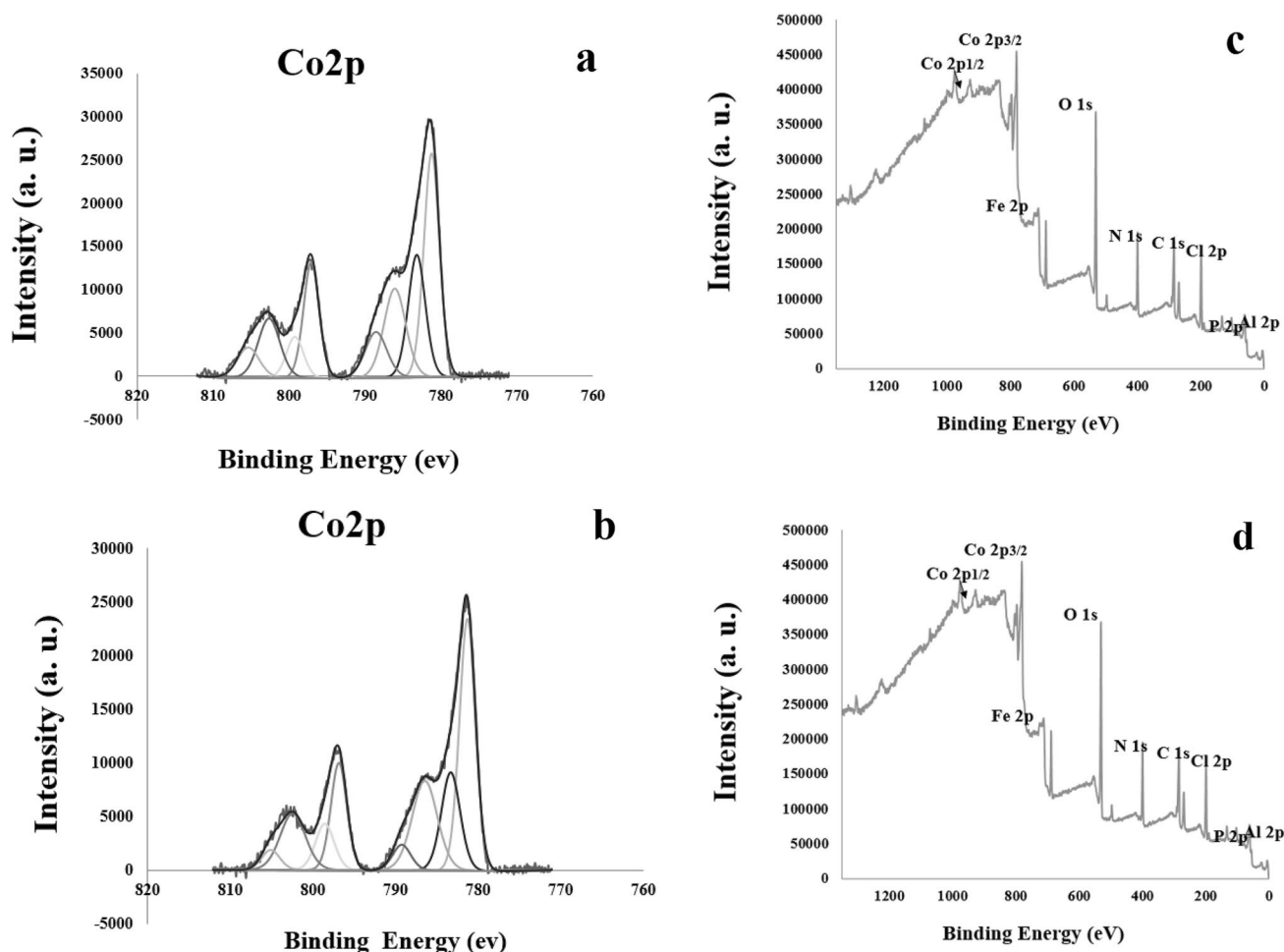
Fig. 10 XPS spectra of the fresh Fe_3O_4@ AMCA-MIL53(Al)-NH_2-Co^{II} NPs (**VI**) (**a**) and the 7th reused Fe_3O_4@ AMCA-MIL53(Al)-NH_2-Co^{II} NPs (**VI**) (**b**) and XPS elemental survey of the fresh Fe_3O_4@ AMCA-MIL53(Al)-NH_2-Co^{II} NPs (**VI**) (**c**) and the 7th reused Fe_3O_4@ AMCA-MIL53(Al)-NH_2-Co^{II} NPs (**VI**) (**d**)
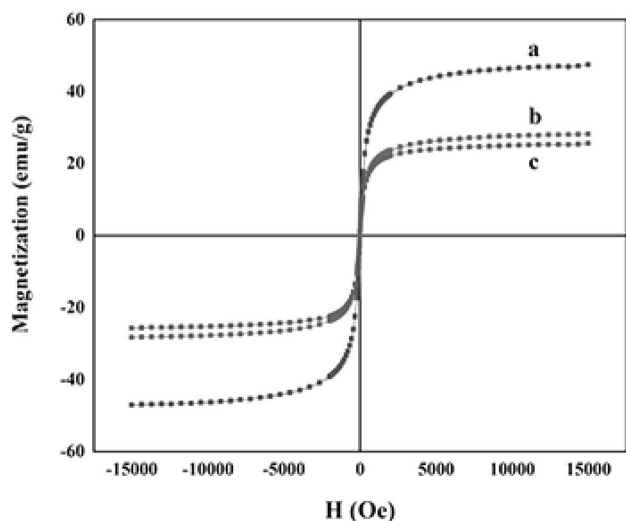
Fig. 11 Magnetization curves of Fe_3O_4@AMCA-MIL53 (Al) NPs (**III**)(a), Fe_3O_4@AMCA-MIL53(Al)-NH_2-Co^{II} NPs (**VI**)(b) and the 7th reused Fe_3O_4@ AMCA-MIL53(Al)-NH_2-Co^{II} NPs (**VI**) (c)

was explored on the model reaction. The obtained data clearly demonstrated that TOF amount of different temperatures (110, 10 and 90 °C) are similar. Accordingly, 90 °C was found to be the best temperature furnishing the cross-coupled product in higher yield comparatively (Table 3, entries 13–16). Due to the essential role of base in this reaction, we turned our attention to determine the best base to achieve higher TOF amount. To reach this goal, the model reaction was performed in the presence of numerous bases. As can be concluded from Table 3, NaOH was found to be the best base, according to its higher TOF amount (Table 3, entries 17–24). Likewise, the effect of catalyst loading and molar ration of iodobenzene/base were also studied. Table 3 clearly showed that the cross-coupling reaction proceeded very effectively using 1/3 molar ratio of iodobenzene/base and 1.08 mol% of catalyst with 42.7×10^{-2} (h^{-1}) and with 14.6×10^{-2} (h^{-1}) amount of TOF, respectively (Table 3, entries 25–30). As a final point, performing the reaction in the presence of

Scheme 2 Devising the Fe$_3$O$_4$@AMCA-MIL53(Al)-NH$_2$-Co[II] NPs(**VI**) for C–O cross-coupling reaction

X= I, Br, Cl

R^1= H, 4-NO$_2$, 4-OMe, 4-Me, 4-CN, 4-NH$_2$, 4-CHO

R^{2}OH/ NaOH, Solvent-free, 90 ºC

R^2= Alkyl, Aryl, Benzyl, Naphthyl

Fe$_3$O$_4$@AMCA-MIL53(Al)-NH$_2$-Co[II] NPs (**VI**)
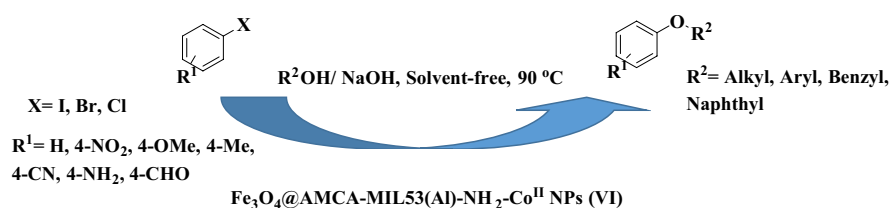
CoCl$_2$·6H$_2$O and CoCl$_2$·6H$_2$O/aminoguanidine with a long period of time is responsible for dropped TOF amounts (Table 3, entries 36–38).

Motivated by the profound initial studies on the optimized reaction conditions and having the obtained results, the substrate scope of the C–O cross-coupling reaction was extended on the cross-coupling reactions of a diversity of aryl halides. It consisted of electron-withdrawing and/or electron-donating substituents with a range of phenols, naphthols, benzylic, allylic, and aliphatic alcohols to generate the desired products. The results are demonstrated in Table 4. As illustrated by the summarized data in Table 4, electron-withdrawing substituents (such as –Cl and –NO$_2$) on the phenyl rings of phenols and benzylic alcohols led to the corresponding products in good to excellent yields (Table 4, entries 2–9 and 19), while electron-donating substituents (such as -OH, -CH$_3$ and -NH$_2$ groups) produced the desired products in low yields after prolonged reaction times (Table 4, entries 10–15 and 20). To further demonstrate the potential application of the present strategy, C–O cross-coupling reactions of α-naphthol and β-naphthol were also investigated. The obtained results noticeably unfolded that using the aforesaid nanostructured catalyst leads to form the desired products in reasonable yields (Table 4, entries 16–17). Interestingly, excellent yields of the corresponding products resulted from the cross-coupling reactions of aliphatic alcohols in the presence of Fe$_3$O$_4$@AMCA-MIL53(Al)-NH$_2$-Co[II] NPs(**VI**) (Table 4, entries 21, 22, 42 and 53). By having assessed the facts of the as-synthesized nanostructured catalyst, now it was time to investigate the effect of various aryl halides on the C–O cross-coupling reaction rate. As envisioned, lower yields were gained with both aryl bromides and aryl chlorides in comparison to aryl iodides due to the better strength of C–Cl and C–Br bonds (Table 4, entries 1, 4, 14, 18 and 22 vs entries 38–42 and 49–53). Moreover, the scope of the present methodology was expanded using variant electron-poor and electron-rich aryl halides (Table 4, entries 23–34, 43–48 and 54–59). The facile reaction of the aryl halides containing electron donated substituents is caused by the more facile reductive elimination step assisted by electron releasing groups (see Scheme 3). Furthermore, to investigate the possible formation of difunctional cross-coupled products, the cross-coupling reactions were performed using a 2/1 molar ratio of iodobenzene/*ortho, meta-* or *para*-hydroxy phenols. Spectroscopic studies reveal the high selectivity of

Fe$_3$O$_4$@AMCA-MIL53(Al)-NH$_2$-Co[II] NPs(**VI**) towards the formation of *mono*-cross-coupled product (Table 4, entries 10–12) (Supporting Information, 4-Phenoxy phenol (**12a**), Page 16).

In the present investigation, the progress of C–O cross-coupling reaction was monitored by disappearance of starting materials and further formation of the desired cross-coupled products on TLC or GC. All of the synthesized compounds were identified and their structures were established by comparison of their melting points and mass spectra with those reported in the literature. In addition, FT-IR spectra of the obtained products did not contain stretching frequencies of O–H bond. Furthermore, the structure of some selected products was determined by surveying the ^{1}HNMR and ^{13}CNMR spectral data (Supporting Information).

By the analogy of the previously reported mechanism in the literature [71, 72] and according to our investigations, a conceivable mechanism was offered in Scheme 3. The cross-coupling reaction is initiated by an in situ reductive of Co[II] complexes to Co[I or 0] species (**I**) in the presence of base (NaOH). (To investigate whether Co[I or 0] species act as catalyst promoter in this reaction, a mixture of the above-mentioned nanostructured catalyst and base was prepared. The in situ generation of Co[0] species was confirmed via surveying the UV–vis.DRS spectrum of the reaction mixture (Fig. 12). The results of UV–vis.DRS spectroscopy reveals the formation of Co[0] species). Whether the oxidative addition of aryl halide or coordination of the heteroatom first happened, it is completely related to the nature of the heteroatom source, ligands, initial oxidation state of the transition metal and also the reaction conditions [28, 29]. Hereupon, based on the obtained results, the coupling may have started with the oxidative addition of aryl halide to low valent Co[0] species (**I**) as the most important step in determining the reaction rate. In the following step, coordination of the heteroatom to Co[II] center (**II**) led to adduct (**IV**) via the formation of intermediate (**III**) (upon the deprotonation under basic conditions). The C–O cross-coupling reaction rate was enhanced in the presence of electron-rich aryl halides. This may be related to the facile extrusion of Co in its reduced form Co[0] from the intermediate (**IV**) in reductive elimination step as the result of more electronegativity of oxygen (according to the above-mentioned results, it is our belief that the oxidative addition may be happened first).

Table 3 Optimization of reaction conditions for C–O cross coupling reaction
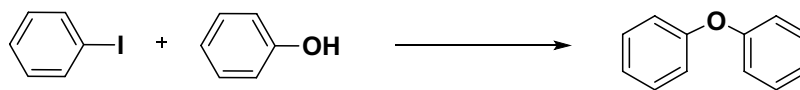
Entry	Catalyst (mol%)	Molar ratio of iodo-benzene/base	Base	Solvent	Temp. (°C)	Time (h)	Isolated Yield (%)	TOF×10^{-2} (h^{-1})
1	–	1/0	–	DMF	100	24	0	0
2	–	1/2	K_2CO_3	DMF	100	24	Trace	0
3	0.27	1/0	-	DMF	100	24	0	0
4	0.27	1/2	K_2CO_3	DMF	100	10	35	12.9
5	0.27	1/2	K_2CO_3	DMSO	100	11	35	11.8
6	0.27	1/2	K_2CO_3	THF	100	15	25	6.2
7	0.27	1/2	K_2CO_3	n-Hexane	100	17	10	2.2
8	0.27	1/2	K_2CO_3	Toluene	100	10	40	14.8
9	0.27	1/2	K_2CO_3	CH_3CN	100	13	20	5.7
10	0.27	1/2	K_2CO_3	EtOH	100	15	20	4.9
11	0.27	1/2	K_2CO_3	H_2O	100	13	25	7.1
12	0.27	1/2	K_2CO_3	–	100	10	40	14.8
13	0.27	1/2	K_2CO_3	–	110	10	40	14.8
14	0.27	1/2	K_2CO_3	–	90	10	40	14.8
15	0.27	1/2	K_2CO_3	–	80	12	30	9.2
16	0.27	1/2	K_2CO_3	–	R.T	24	0	0
17	0.27	1/2	Li_2CO_3	–	90	13	35	9.9
18	0.27	1/2	$NaHCO_3$	–	90	12	30	9.2
19	0.27	1/2	K_3PO_4	–	90	8	50	23.1
20	0.27	1/2	KOH	–	90	10	45	16.6
21	0.27	1/2	TETA	–	90	8	50	23.1
22	0.27	1/2	NEt_3	–	90	9	40	16.4
23	0.27	1/2	Ethylenediamine	–	90	11	50	16.8
24	0.27	1/2	NaOH	–	90	7	60	31.7
25	0.27	1/3	NaOH	–	90	6.5	75	42.7
26	0.27	1/4	NaOH	–	90	6.5	75	42.7
27	0.54	1/3	NaOH	–	90	6	80	24.7
28	0.81	1/3	NaOH	–	90	6	85	17.4
29	**1.08**	**1/3**	**NaOH**	**–**	**90**	**6**	**95**	**14.6**
30	1.35	1/3	NaOH	–	90	6	95	11.7
31[a]	0.04(g)	1/3	NaOH	–	90	24	10	–
32[b]	0.04(g)	1/3	NaOH	–	90	24	5	–
33[c]	0.04(g)	1/3	NaOH	–	90	24	Trace	–
34[d]	0.04(g)	1/3	NaOH	–	90	24	Trace	–
35[e]	0.04(g)	1/3	NaOH	–	90	24	Trace	–
36[f]	0.04(g)	1/3	NaOH	–	90	24	Trace	–
37[g]	1.08	1/3	NaOH	–	90	24	0	0
38[h]	1.08	1/3	NaOH	–	90	24	30	1.1

Bold indicates the optimized reaction conditions which obtained after performing a series experiments on the model reaction

TETA triethylenetetramine

[a] Reaction was performed in the presence of Fe_3O_4NPs

[b] Reaction was performed in the presence of NH_2-MIL53(Al)(**I**)

[c] Reaction was performed in the presence of AMCA-MIL53(Al)(**II**)

[d] Reaction was performed in the presence of Fe_3O_4@AMCA-MIL53(Al) NPs(**III**)

[e] Reaction was performed in the presence of Fe_3O_4@AMCA-MIL53(Al)-Ethephon (**IV**)

[f] Reaction was performed in the presence of Fe_3O_4@AMCA-MIL53(Al)-NH_2(**V**)

[g] Reaction was performed in the presence of $CoCl_2 \cdot 6H_2O$

Table 3 (continued)

[h]Reaction was performed in the presence of CoCl$_2$·6H$_2$O and 2.16 mol% of aminoguanidine

Scheme 3 Proposed mechanism for C–O cross-coupling reaction in the presence of Fe$_3$O$_4$@AMCA-MIL53(Al)-NH$_2$-Co^{II} NPs (**VI**)
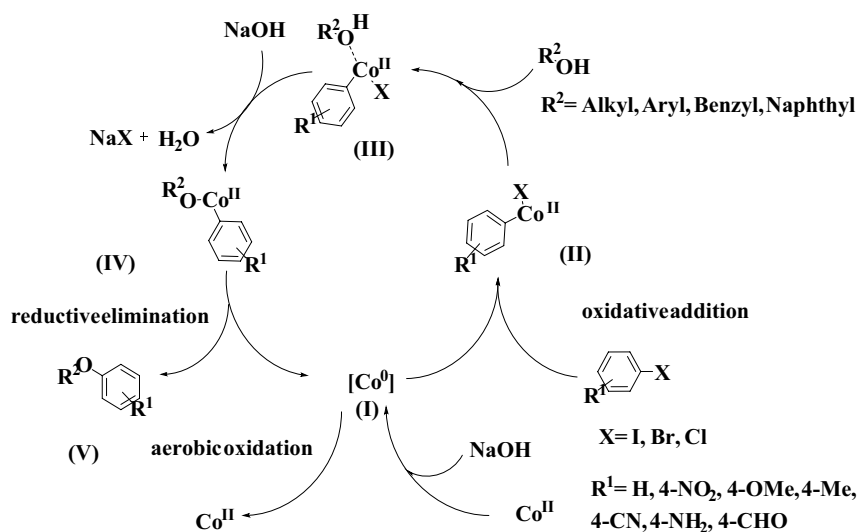


The desired product (**V**) was obtained through the reductive elimination process along with the regeneration of the active catalytic species Co^0 (**I**) which took place in the next cycle. Eventually, the catalytic cycle was completed through the oxidation of the active Co^0 species to Co^{II} complexes under aerobic conditions [33]. However, an alternative pathway via coordination of the C–O source to the Co^0 center (**I**), cannot be completely ruled out. There is no doubt that a more detailed study is required to completely understand the mechanism of the C–O cross-coupling reaction in the presence of cobalt species.

From the green chemistry viewpoint, the long term-durability of heterogeneous catalyst is one of the most important as which makes them useful for commercial applications. To explore the reusability of the synthesized Fe$_3$O$_4$@AMCA-MIL53(Al)-NH$_2$-Co^{II} NPs(**VI**), the model reaction of C–O cross-coupling reaction was performed under the optimized reaction conditions. At the end of each reaction which was monitored by TLC, the nanostructured catalyst was separated by means of an external magnetic field, washed with water, ethanol and dried at 50 °C overnight to remove residual solvents. The recycled nanostructured catalyst could be directly reused for a subsequent reaction run without further purification. The recycling efficiency has been plotted in Fig. 13. As illustrated in Fig. 13, Fe$_3$O$_4$@AMCA-MIL53(Al)-NH$_2$-Co^{II} NPs(**VI**) was reused seven times without a conspicuous loss of activity in the C–O cross-coupling reaction. The observed decrease in the yield could be related to the blocking of some pores by organic segments as well as negligible leaching of cobalt species during recycling process. The identical results in each cycle unambiguously infer

Fe$_3$O$_4$@AMCA-MIL53(Al)-NH$_2$-Co^{II} NPs(**VI**) is not only active enough for C–O cross-coupling reaction but also is very stable even after several recycle runs.

To gain a deep insight into the stability of Fe$_3$O$_4$@AMCA-MIL53(Al)-NH$_2$-Co^{II} NPs(**VI**) after seven cycles in the C–O cross-coupling reaction, any structural changes of the nanostructured catalyst were investigated by FT-IR, XRD, BET, TEM, FE-SEM, EDX, TGA, XPS, VSM and ICP-OES techniques.

Through surveying the FT-IR spectra of the 7th reused nanostructured catalyst, the conclusion could be derived that all of the characteristic absorption bands are well preserved in terms of the shapes, positions, intensities, and frequencies even after seven recycle runs (Fig. 1g). Additionally, it is interesting to note that no significant broadening or shifting was observed in the typical diffraction peaks of the XRD pattern of the 7th reused nanostructured catalyst when compared with the XRD pattern of the fresh Fe$_3$O$_4$@AMCA-MIL53(Al)-NH$_2$-Co^{II} NPs(**VI**), according to the data summarized in Fig. 2e. Likewise, the nitrogen adsorption–desorption isotherm of the 7th recovered Fe$_3$O$_4$@AMCA-MIL53(Al)-NH$_2$-Co^{II} NPs(**VI**) was scrutinized and the results showed that the BET surface area decreased during the reusing process owing to the blockage of some pores by organic segments or solvents (Table 5 and Fig. 3d). Satisfyingly, the TEM images of Fe$_3$O$_4$@AMCA-MIL53(Al)-NH$_2$-Co^{II} NPs(**VI**) after 7 recovering from the C–O cross-coupling reaction demonstrated that no agglomeration or increase in the particle size was observed, according to the data illustrated in Figs. 4c and 5b. Moreover, the FE-SEM image of the 7th reused nanostructured catalyst confirmed

Table 4 Scope and functional group tolerance of Fe_3O_4@AMCA-MIL53(Al)-NH_2-Co^{II} NPs(**VI**) catalyzed the C–O cross-coupling reaction
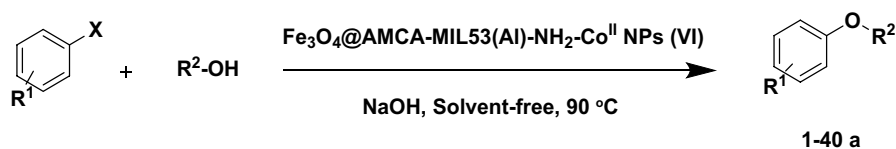
Entry	R^1	X	R^2	Product	Time (h)/ isolated yield (%)
1	H	I	C_6H_5	**1a**	6/95
2	H	I	2-ClC_6H_4	**2a**	6/90
3	H	I	3-ClC_6H_4	**3a**	7/75
4	H	I	4-ClC_6H_4	**4a**	6/90
5	H	I	2,3-Di-ClC_6H_3	**5a**	6/95
6	H	I	2,6-Di-ClC_6H_3	**6a**	5/95
7	H	I	2-$O_2NC_6H_4$	**7a**	6/90
8	H	I	4-$O_2NC_6H_4$	**8a**	6/95
9	H	I	2,4-Di-$O_2NC_6H_3$	**9a**	6/95
10	H	I	2-HOC_6H_4	**10a**	9/35
11	H	I	3-HOC_6H_4	**11a**	9/50
12	H	I	4-HOC_6H_4	**12a**	9/60
13	H	I	2-$H_3CC_6H_4$	**13a**	12/60
14	H	I	4-$H_3CC_6H_4$	**14a**	10/75
15	H	I	3,5-Di-$H_3CC_6H_3$	**15a**	13/50
16	H	I	1-Naphthyl	**16a**	7/80
17	H	I	2-Naphthyl	**17a**	7/75
18	H	I	Benzyl	**18a**	4/95
19	H	I	4-Cl-Benzyl	**19a**	4/95
20	H	I	4-CH3-Benzyl	**20a**	4/90
21	H	I	Cyclo hexyl	**21a**	6/90
22	H	I	Butyl	**22a**	6/95
23	4-NO_2	I	C_6H_5	**23a**	8/50
24	4-NO_2	I	4-ClC_6H_4	**24a**	8/65
25	4-NO_2	I	4-$H_3CC_6H_4$	**25a**	10/60
26	4-CN	I	C_6H_5	**26a**	8/55
27	4-CN	I	4-ClC_6H_4	**27a**	8/60
28	4-CN	I	4-$H_3CC_6H_4$	**28a**	10/60
29	4-CH_3	I	C_6H_5	**29a**	7/60
30	4-CH_3	I	4-ClC_6H_4	**30a**	6/60
31	4-CH3	I	4-$H_3CC_6H_4$	**31a**	9/60
32	4-OCH_3	I	C_6H_5	**32a**	7/70
33	4-OCH_3	I	4-ClC_6H_4	**33a**	6/70
34	4-OCH_3	I	4-$H_3CC_6H_4$	**34a**	9/60
35	4-CHO	I	C_6H_4	**35a**	7/90
36	4-CHO	I	4-ClC_6H_4	**36a**	6/90
37	4-CHO	I	4-$H_3CC_6H_4$	**37a**	8/90
38	H	Br	C_6H_5	**1a**	6.5/95
39	H	Br	4-ClC_6H_4	**4a**	6.5/90
40	H	Br	4-$H_3CC_6H_4$	**14a**	14/95
41	H	Br	Benzyl	**18a**	5/90
42	H	Br	Butyl	**22a**	6/75

Table 4 (continued)

Entry	R^1	X	R^2	Product	Time (h)/ isolated yield (%)
43	4-NH2	Br	C$_6$H$_5$	**38a**	6/95
44	4-NH$_2$	Br	4-ClC$_6$H$_4$	**39a**	6/95
45	4-NH$_2$	Br	4-H$_3$CC$_6$H$_4$	**40a**	12/95
46	4-CN	Br	C$_6$H$_5$	**26a**	7/95
47	4-CN	Br	4-ClC$_6$H$_4$	**27a**	7/95
48	4-CN	Br	4-H$_3$CC$_6$H$_4$	**28a**	14/95
49	H	Cl	C$_6$H$_5$	**1a**	10/55
50	H	Cl	4-ClC$_6$H$_4$	**4a**	10/60
51	H	Cl	4-H$_3$CC$_6$H$_4$	**14a**	13/45
52	H	Cl	Benzyl	**18a**	9/45
53	H	Cl	Butyl	**22a**	12/35
54	4-NH$_2$	Cl	C$_6$H$_5$	**38a**	10/55
55	4-NH$_2$	Cl	4-ClC$_6$H$_4$	**39a**	10/60
56	4-NH$_2$	Cl	4-H$_3$CC$_6$H$_4$	**40a**	13/45
57	4-CN	Cl	C$_6$H$_5$	**26a**	13/40
58	4-CN	Cl	4-ClC$_6$H$_4$	**27a**	13/45
59	4-CN	Cl	4-H$_3$CC$_6$H$_4$	**28a**	15/30
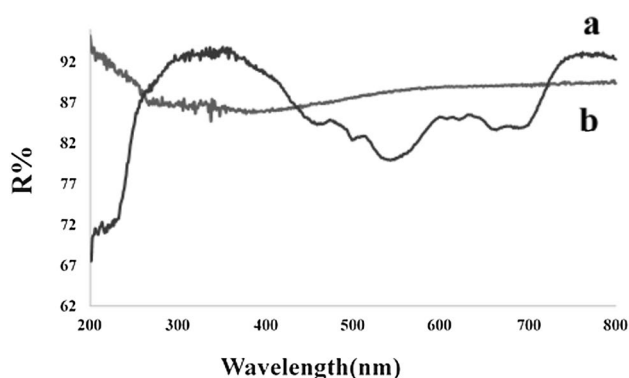
Fig. 12 UV–vis.DRS spectra of cobalt(II) chloride (a) and Fe$_3$O$_4$@ AMCA-MIL53(Al)-NH$_2$-Co^{II} NPs(**VI**) (b)
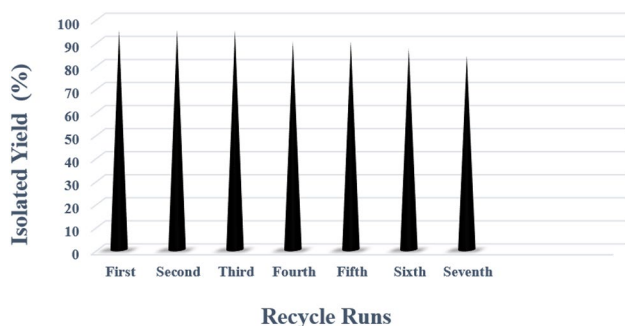
Fig. 13 C–O cross-coupling reaction in the presence of the reused Fe$_3$O$_4$@AMCA-MIL53(Al)-NH$_2$-Co^{II} NPs(**VI**)

that no agglomeration or changes in the shape and morphology of Fe$_3$O$_4$@AMCA-MIL53(Al)-NH$_2$-Co^{II} NPs(**VI**) was observed even after 7 recycle runs (Fig. 6d). Additionally, the stability of Fe$_3$O$_4$@AMCA-MIL53(Al)-NH$_2$-Co^{II} NPs(**VI**) was corroborated via probing the EDX image of the 7th reused nanostructured catalyst. The results summarized in Fig. 7 truly exhibited the presence of C, O, N, P, Fe, Co, Al, and Cl elements in the Fe$_3$O$_4$@AMCA-MIL53(Al)-NH$_2$-Co^{II} NPs(**VI**) nanostructure composition (Fig. 7b). Comparing the TGA thermograms of the fresh and the 7th reused nanostructured catalyst expressed that no significant difference was observed in the decomposition patterns, as it is evident from Fig. 9g, f. The only observed difference was related to decreasing the percentage weight loss from 23% in the fresh nanostructured catalyst to 22.5% after seven cycles in the C–O cross-coupling reaction. Moreover, the XPS spectrum of the 7th reused Fe$_3$O$_4$@AMCA-MIL53(Al)-NH$_2$-Co^{II} NPs(**VI**) purely authenticated that the oxidation state of Co species was preserved even after seven recycle in the C–O cross-coupling reaction (Fig. 10b, d). As can be concluded from the magnetization curves (Fig. 11), the saturation magnetization value of Fe$_3$O$_4$@AMCA-MIL53(Al)-NH$_2$-Co^{II} NPs(**VI**) decreased from 28.05 to 25.2 after seven recycle runs in the C–O cross-coupling reaction. The observed decrease may be related to the blockage of some pores with organic segments. In other words, due to repositioning of the organic moieties around the Fe$_3$O$_4$ MNPs, the magnetization saturation values decreased (Fig. 11c).

The ICP-OES technique was applied to estimate the exact amount of cobalt in the fresh and the 7th reused $Fe_3O_4@$ AMCA-MIL53(Al)-NH_2-Co^{II} NPs(**VI**). According to the obtained data, 0.43 and 0.41 mmol of cobalt were anchored on 1.000 g of the fresh and the 7th reused nanostructured catalyst from the C–O cross-coupling reaction, respectively. These results clearly proved that the negligible amount of cobalt was leached from the surface of the mesoporous nanostructured catalyst during the recycling process.

Based on the obtained data from FT-IR, XRD, BET, TEM, FE-SEM, EDX, TGA, XPS, VSM, and ICP-OES analysis, there is no doubt that the nanostructured catalyst is stable from the viewpoint of physical properties including functional groups, crystallographic structure, shape, morphology, particle size, thermal stability, oxidation state, and magnetic properties even after 7 recycle runs.

3.3 Heterogeneity Studies

In order to determine the homogeneity or heterogeneity nature of the catalyst in the C–O cross-coupling reaction, a series of experiments such as hot filtration test, kinetics study, and poisoning test were done and the results are discussed as follows.

3.3.1 Hot Filtration Test

The hot filtration test is one of the important methods to assess the nature of the catalytic species based on the comparison of the reaction progress before and after removal of the solid catalyst. To this point, the model C–O cross-coupling reaction was performed under the optimal conditions. Mid-way through each reaction (3 h), the nanostructured catalyst was separated from the reaction media. Subsequently, the remaining mixture was permitted to continue without a catalyst for an additional 3 h. The reaction progress was monitored by GC before and after the separation. No significant increase in the yield of the desired product was observed even after an extended time. The hot filtration test result is strongly evident that no or negligible leaching of active species (5.1×10^{-6} mol%, according to the ICP-OES analysis) from the surface of $Fe_3O_4@$AMCA-MIL53(Al)-NH_2-Co^{II} NPs(**VI**) occurred during the reaction. Since quick re-deposition of soluble active species occurred prior or during the separation process, a negative hot filtration test is not sufficient to declare a catalyst to be truly heterogeneous, while a positive hot filtration test confirmed the homogeneity nature of the catalyst. Accordingly, due to the difficulties noted with the hot filtration test and to confirm the homogeneity or heterogeneity nature of the catalyst, further experiments are required.

3.3.2 Kinetics Study

The appearance of a typical induction period in the catalytic reaction is one of the characteristics of the kinetic studies which exhibited the presence of homogeneous precatalyst in the reaction media. Hence, a kinetic study was performed to discern the homogeneity or heterogeneity nature of the catalyst. To conduct the test, the model C–O cross-coupling reaction was studied under the optimized reaction conditions. The reactions progress was followed using gas chromatography (GC). No induction period was observed, as it is evident in Fig. 14. These results suggested that there are no soluble catalytic species in the reaction mixture and the $Fe_3O_4@$AMCA-MIL53(Al)-NH_2-Co^{II} NPs(**VI**) nanostructured catalyst presumably had a heterogeneous nature.

3.3.3 Poisoning Test

To further explore the true nature of the as-synthesized nanostructured catalyst, a poisoning test was performed. In order to do so, the model C–O cross-coupling reaction was carried out under the optimized reaction conditions in the presence and in the absence of ethylenediaminetetraacetic acid (EDTA) as an effective scavenger to capture the homogeneous cobalt species. The high affinity of EDTA to grab the soluble Co^{II} ions leads to the formation of a stable complex(**VII**) (Scheme 4) which deactivates the leached out cobalt species. Therefore, if the reactions stopped in the presence of EDTA, it can be concluded that the leached out cobalt species promote this coupling reaction and no significant decrease in the yield of the reaction confirmed the heterogeneity nature of the framework nanostructured catalyst. In this regards, the reaction progress was monitored by
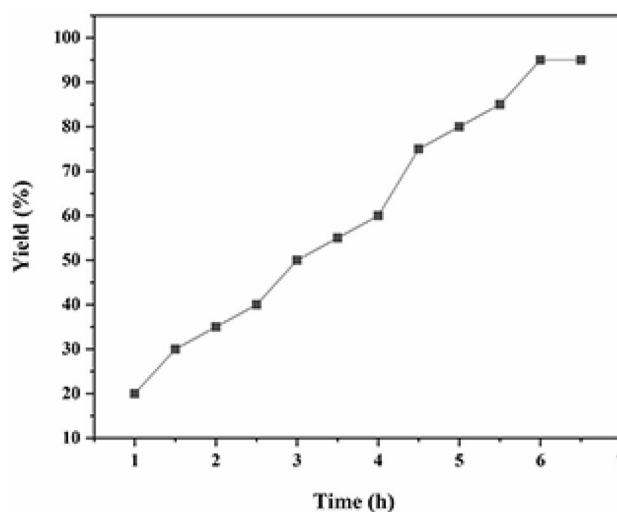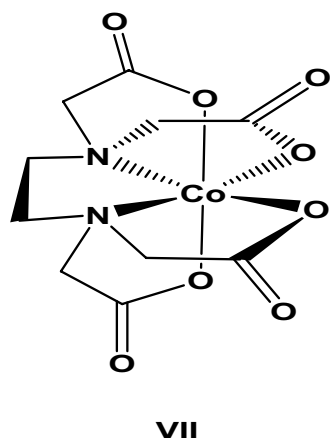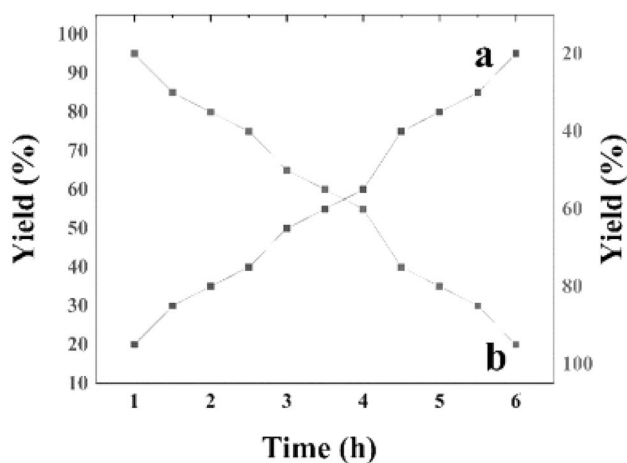

Fig. 14 Time-dependent correlation of the product yield in the kinetic study

Scheme 4 The chemical structure of the Co(EDTA)^{II} complex(**VII**)

Fig. 15 Time-dependent correlation of the yield of model C–O cross-coupling reaction in the presence and in the absence of EDTA (ethylenediaminetetraacetic acid)

GC and the results are demonstrated in Fig. 15. In accordance with these results, affording the corresponding product without any detectable decrease in the yield of the reaction, clearly corroborated that no leaching of cobalt ions takes place during the reaction and the reaction arguably proceed in a heterogeneous pathway. Considering these results, it is now beyond any doubt that the Fe$_3$O$_4$@AMCA-MIL53(Al)-NH$_2$-Co^{II} NPs(**VI**) nanostructured catalyst is purely heterogeneous in nature under the described reaction conditions.

Finally, to show the merit of the current protocol with respect to other reported methods in the literature, the catalytic activity of Fe$_3$O$_4$@AMCA-MIL53(Al)-NH$_2$-Co^{II} NPs(**VI**) was compared with some of the previously reported catalysts in the C–O cross-coupling reaction (Table 5). Among the listed catalysts in Table 5, the current method combatively affords a truly green process and is much superior to almost all of the well-known catalyst systems. This superiority can be described in terms of the reaction time (entries 1–2 and 5–6), and temperature (entries 2 and 5–6). Other criteria include solvent (entries 1–2 and 5–6), recovery and reusability (entry 1) as well as price (entries 3–4) and finally toxicity (entries 1–4 and 6).

4 Conclusion

In the present study, Fe$_3$O$_4$@AMCA-MIL53(Al)-NH$_2$-Co^{II} NPs were synthesized as a new magnetic nanostructured catalyst based on the metal–organic framework structures. Characterization results from various spectroscopic and microscopic techniques such as FT-IR, XRD, BET, TEM, FE-SEM, EDX, EDX-mapping, TGA, XPS, VSM, ICP-OES, and CHN showed the superparamagnetic nature of Fe$_3$O$_4$@AMCA-MIL53(Al)-NH$_2$-Co^{II} NPs with a mean size range of 10–30 nm which is core–shell-like in shape. By using this nanostructured catalyst, the C–O cross-coupling reaction of diverse aryl halides (containing electron-withdrawing and electron-donating substituents) with a range of phenols,

Table 5 Comparison of the catalytic activity of Fe$_3$O$_4$@AMCA-MIL53(Al)-NH$_2$-Co^{II} NPs(**VI**) with some literature precedents for C–O cross-coupling reaction

Entry	Catalyst	Solvent	Temp (°C)	Time (h)/ isolated yield (%)	Reusability	Ref
1	CuI/Metformin	CH$_3$CN	60	8/96	–	[73]
2	Meso-N-C^a 50 mg/CuI	DMSO	100	24/85	4	[74]
3	^{b}AT-Nano CP Pd0	H$_2$O	60	1/98	8	[27]
4	Fe$_3$O$_4$@pph$_2$-Pd0	H$_2$O	80	1.5/93	6	[75]
5	Ferrous chamosite	DMF	110	12/97		[76]
6	Maghemite-Cu NPs	DMF	130	24/87	6	[77]
7	Fe$_3$O$_4$@AMCA-MIL53 (Al)-NH$_2$-Co^{II} NPs(**VI**)	–	90	6/95	7	Present study

^{a}Mesoporous nitrogen-doped carbon

^{b}Activated Nano Clinoptilolite

naphthols, benzylic, allylic, and aliphatic alcohols gave the corresponding products under mild reaction conditions. The present heterogeneous nanostructured catalyst expands the scope of the substrate by reducing reaction time and temperature to avoid using palladium (due to its high cost and toxicity) and copper(I) catalysts (due to its instability). Furthermore, Fe_3O_4@AMCA-MIL53(Al)-NH_2-Co^{II} NPs can be simply separated magnetically from the reaction mixture and reused at least seven times with trace cobalt leaching without a significant reduction in the yields of the desired products. Moreover, the spectroscopic and microscopic studies of the 7th reused catalyst displayed considerable stability of the Fe_3O_4@AMCA-MIL53(Al)-NH_2-Co^{II} NPs under the reaction conditions. Affording good to excellent yields of the C–O cross-coupled products without the need for any special conditions underlines the potential of using cobalt as a readily available, low-cost, non-toxic, and efficient catalyst for C–O as well as C–C cross-coupling reactions. Further studies are underway in our laboratory to extend this nanostructured catalyst to other cross-coupling reactions.

Compliance with Ethical Standards

Conflict of interest There is no conflict of interest for each contributing author.

References

1. Negwar M (1994) Organic-chemical drugs and their synonyms. Akademie Verlag/VCH Publishers, New York
2. Corbet JP, Mignani G (2006) Chem Rev 106:2651
3. Ritleng V, Sirlin C, Pfeffer M (2002) Chem Rev 102:1731
4. Muci AR, Buchwals SL (2002) Top Curr Chem 219:131
5. Diederich F, de Meijere A (2004) Metal-catalyzed cross-coupling reactions. Wiley-VCH, Weinheim
6. Campeau LC, Fagnou K (2006) Chem Commun. https://doi.org/10.1039/B515481M
7. Daugulis O, Zaitsev VG, Shabashou D, Pham QN, Lazareva A (2006) Synlett 20:3382
8. Godula K, Sames S (2006) Science 312:67
9. Dick AR, Sanford MS (2006) Tetrahedron 62:2439
10. Alberico D, Scott ME, Lautens M (2007) Chem Rev 107:174
11. Seregin IV, Gevorgyan V (2007) Chem Soc Rev 36:1173
12. Davies HML, Manning JR (2008) Nature 451:417
13. Monnier F, Taillefer M (2009) Angew Chem Int Ed 48:6954
14. Evano G, Blanchard N, Toumi M (2008) Chem Rev 108:3054
15. Sambiagio C, Marsden SP, Blacker AJ, McGowan PC (2014) Chem Soc Rev 43:3525
16. Lindley J (1984) Tetrahedron 40:1433
17. Ley SV, Thomas AW (2003) Angew Chem Int Ed 42:5400
18. Ley SV, Thomas AW (2003) Angew Chem 115:5558
19. Sawyer JS (2000) Tetrahedron 56:5045
20. Frlan R, Kikelj D (2006) Synthesis 14:2271
21. Zhang H, Ruiz-Castillo P, Buchwald SL (2018) Org Lett 20:1580
22. MacQueen PM, Tassone JP, Diaz C, Stradiotto M (2018) J Am Chem Soc 140:5023
23. Sun H, Sun Y, Tian X, Zhao Y, Qi X (2013) Asian J Chem 25:6189
24. Singh AS, Shendage SS, Nagarkar JM (2013) Tetrahedron Lett 54:6319
25. Singh AS, Shendage SS, Nagarkar JM (2014) Tetrahedron Lett 55:4917
26. Miaoa T, Wang L (2007) Tetrahedron Lett 48:95
27. Baghbanian SM, Yadollahy H, Tajbakhsh M, Farhangb M, Biparva P (2014) RSC Adv 4:62532
28. Mullick K, Biswas S, Kim C, Ramprasad R, Angeles-Boza AM, Suib SL (2017) Inorg Chem 56:10290
29. Saha P, Ashif Ali M, Ghosh P, Punniyamurthy T (2010) Org Biomol Chem 8:5692
30. Yang L, Jin Y, Fang X, Cheng Z, Zhou Z (2017) Ind Eng Chem Res 56:14182
31. Zhao L, Zheng K, Tong J, Jin J, Shen C (2019) Catal Lett 149:2607
32. Fang Q, Cheng Q, Xu H, Xuan S (2014) Dalton Trans 43:2588
33. Nicholas KM (1987) Acc Chem Res 20:207
34. Mohammadinezhad A, Akhlaghinia B (2017) Green Chem 19:5625
35. Jahanshahi R, Akhlaghinia B (2017) Catal Lett 147:2640
36. Razavi N, Akhlaghinia B, Jahanshahi R (2017) Catal Lett 147:360
37. Zarghani M, Akhlaghinia B (2016) Bull Chem Soc Jpn 89:1192
38. Ghasemzadeh MS, Akhlaghinia B (2019) Aust J Chem 72:674
39. Cheng X, Zhang A, Hou K, Liu M, Wang Y, Song C, Zhang G, Guo X (2013) Dalton Trans 42:13698
40. Alqadami AA, Naushad Mu, Alothman ZA, Ghfar AA (2017) ACS Appl Mater Interfaces 9:36026
41. Yaghi OM, O'Keeffe M, Ockwig NW, Chae HK, Eddaoudi M, Kim J (2003) Nature 423:705
42. Jin M, Mou ZL, Zhang RL, Liang SS, Zhang ZQ (2017) Biosens Bioelectron 91:162
43. Cohen SM (2012) Chem Rev 112:970
44. Stock N, Biswas S (2012) Chem Rev 112:933
45. Kitaura R, Kitagawa S, Kubota Y, Kobayashi TC, Kindo K, Mita Y, Matsuo A, Kobayashi M, Chang HC, Ozawa TC, Suzuki M, Sakata M, Takata M (2002) Science 298:2358
46. Ferey G, Cheetham AK (1999) Science 283:1125
47. Lu G, Li S, Guo Z, Farha OK, Hauser BG, Qi X, Wang Y, Wang X, Han S, Liu X, DuChene JS, Zhang H, Zhang Q, Chen X, Ma J, Loo SCJ, Wei WD, Yang Y, Hupp J, Huo F (2012) Nat Chem 4:310
48. Cadiau A, Adil K, Bhatt PM, Belmabkhout Y, Eddaoudi M (2016) Science 353:137
49. Cui X, Chen K, Xing H, Yang Q, Krishna R, Bao Z, Wu H, Zhou W, Dong X, Han Y, Li B, Ren Q, Zaworotko MJ, Chen B (2016) Science 353:141
50. Gascon J, Aktay U, Hernandez-Alonso MD, van Klink GPM, Kapteijn F (2009) J Catal 261:75
51. Ahnfeldt T, Gunzelmann D, Loiseau T, Hirsemann D, Senker J, Fé rey G, Stock N (2009) Inorg Chem 48:3057
52. Naushad M, Ahamad T, Al-Maswari BM, Alqadami AA, Alshehri SM (2017) Chem Eng J 330:1351
53. Buckingham D, Jones D (1965) Inorg Chem 4:1387
54. Mahmoud ME, Abdelwahab MS, Fathallah EM (2013) Chem Eng J 223:318
55. Liu J, Zou X, Liu C, Cai K, Zhao N, Zheng W, Zhu G (2016) CrystEngComm 18:525
56. Yang Y, Wang W, Li H, Jin X, Wang H, Zhang L, Zhang Y (2017) Mater Lett 197:17
57. Alqadami AA, Ali Khan M, Siddiqui MR, Abdullah Alothman Z (2018) Microporous Mesoporous Mater 261:198

58. Mubashir M, Fong YY, Keong LK (2018) Sep Purif Technol 199:140
59. Rostamnia S, Jafari M (2017) Appl Organomet Chem 31:3584
60. Mizuno J (1960) J Phys Soc Jpn 15:1412
61. Chen XY, Vinh-Thang H, Rodrigue D, Kaliaguine S (2012) Ind Eng Chem Res 51:6895
62. Abedini R, Omidkhah M, Dorosti F (2014) RSC Adv 4:36522
63. Bromberg L, Su X, Hatton TA (2013) ACS Appl Mater Interfaces 5:5468
64. Feijani EA, Tavasoli A, Mahdavi H (2015) Ind Eng Chem Res 54:12124
65. Liu L, Tai X, Zhou X, Liu L (2017) CRCU 33:231
66. Chen XY, Hoang VT, Rodrigue D, Kaliaguine S (2013) RSC Adv 3:24266
67. Hashemzadeh A, Amini MM, Tayebee R, Sadeghian A, Durndell LJ, Isaacs MA, Osatiashtiani A, Parlett CMA, Lee AF (2017) Mol Catal 440:96
68. Carrara C, Irusta S, Lombardo E, Cornaglia L (2001) Appl Catal A 217:275
69. Chen Y, Zhao S, Liu Z (2015) Phys Chem Chem Phys 17:14012
70. Yong-Hao Tan B, Yong-Chua T (2015) Synlett 26:1697
71. Wong YC, Jayanth TT, Cheng CH (2006) Org Lett 8:5613
72. Ibrahim H, Dabai Bala M (2015) J Organomet Chem 794:301
73. Ghorbani-Vaghei R, Hemmati S, Veisi H (2013) Tetrahedron Lett 54:7095
74. Zhang P, Yuan J, Li H, Liu X, Xu X, Antonietti M, Wang Y (2013) RSC Adv 3:1890
75. Zolfigol MA, Khakyzadeh V, Moosavi-Zare AR, Rostami A, Zare A, Iranpoor N, Beyzavi MH, Luque R (2013) Green Chem 15:2132
76. Arundhathi R, Sreedhar B, Parthasarathy G (2011) Appl Clay Sci 51:131
77. Sharma RK, Gaur R, Yadav M, Rathi AK, Pechousek J, Petr M, Zboril R, Gawande MB (2015) Chem Cat Chem 7:3495